A&A, 701, A208 (2025)
https://doi.org/10.1051/0004-6361/202554986

Astronomy & Astrophysics

X-SHYNE: X-Shooter spectra of young exoplanet analogs

II. Presentation and analysis of the full library★

S. Petrus[1,2,3,4★★,★★★], G. Chauvin[5,6], M. Bonnefoy[4], P. Tremblin[7], C. Morley[8], B. Charnay[9], G. Suarez[10], J. Gagné[11,12], P. Palma-Bifani[6,9], A. Denis[13], M. Ravet[4], A. Bayo[14], B. Bézard[9], B. Biller[15], P. Delorme[4], J. Faherty[10], J.-M. Goyal[16,17], K. Hoch[18], K. Hoy[2,3], J.-S. Jenkins[2,19], A.-M. Lagrange[9], B. Lavie[20], M. C. Liu[21], E. Manjavacas[18,22], G.-D. Marleau[23,5,25], M. McElwain[1], P. Mollière[5], C. Mordasini[23,24], M. Phillips[21], P. Rojo[26], Z. Zhang[27,28★★★★], and A. Zurlo[2,3]

(Affiliations can be found after the references)

Received 1 April 2025 / Accepted 30 May 2025

ABSTRACT

Characterizing exoplanets' spectra is a crucial step in understanding the chemical and physical processes shaping their atmospheres and constraining their formation and evolutionary history. The X-SHYNE library is a homogeneous sample of 43 medium-resolution ($R_\lambda \sim 8000$) infrared (0.3–2.5 μm) spectra of young (<500 Myr), low-mass (<20 M_{Jup}), and cold (T_{eff} ~600–2000 K) isolated brown dwarfs and wide-separation companions observed with the VLT/X-Shooter instrument. To characterize our targets, we performed a global comparative analysis. We first applied a semiempirical approach. By refining their age and bolometric luminosity, we derived key atmospheric and physical properties, such as T_{eff}, mass, surface gravity (g), and radius, using the evolutionary model `COND03`. These results were then compared with the results from a synthetic analysis based on three self-consistent atmospheric models: the cloudy models `Exo-REM` and `Sonora Diamondback`, and the cloudless model `ATMO`. To compare our spectra with these grids we used the Bayesian inference code `ForMoSA`. We found similar L_{bol} estimates between both approaches, but an underestimated T_{eff} from the cloudy models, likely due to a lack of absorbers that could dominate the J and H bands of early L. We also observed a discrepancy in the log(g) estimates, which are dispersed between 3.5 and 5.5 dex for mid-L objects. We interpret this as a bias caused by a range of rotational velocities leading to cloud migration toward equatorial latitudes, combined with a variety of viewing angles that result in different observed atmospheric properties (cloud column densities, atmospheric pressures, etc.). This interpretation is supported by the correlation of the color anomaly Δ(J–K) of each object with log(g) and the parameter f_{sed} that drives the sedimentation of the clouds. Finally, while providing robust estimates of [M/H] and C/O for individual objects remains challenging, the X-SHYNE library globally suggests solar values that are consistent with a formation via stellar formation mechanisms. This study highlights the strength of homogeneous datasets in performing comparative analyses, reducing the impact of systematics, and ensuring robust conclusions while avoiding overinterpretation.

Key words. methods: data analysis – techniques: imaging spectroscopy – planets and satellites: atmospheres – brown dwarfs

1. Introduction

For the past 20 years, it has been possible to obtain spectra of massive planetary-mass companions (>3 M_{Jup}) at wide separations (>15 AU) observed through direct imaging, mostly in the near-infrared. Initially, this was achieved from the ground at a low resolution with high-contrast spectro-imagers such as VLT/SPHERE ($R_\lambda \sim 50$; Beuzit et al. 2019), Keck/GPI ($R_\lambda \sim 66$; Macintosh et al. 2014), and Subaru/SCExAO+CHARIS ($R_\lambda \sim 80$; Jovanovic et al. 2016, Peters-Limbach et al. 2012), at a medium resolution with integral field spectrographs such as Keck/OSIRIS ($R_\lambda \sim 8000$; Larkin et al. 2006), VLT/SINFONI ($R_\lambda \sim 4000$; Eisenhauer et al. 2003), or now VLT/ERIS ($R_\lambda \sim 8000$; Davies et al. 2023), and with interferometry using VLTI/GRAVITY ($R_\lambda \sim 500$–4000; GRAVITY Collaboration 2017) and VLTI/MATISSE ($R_\lambda \sim 500$; Lopez et al. 2022), and finally at a high resolution with projects such as VLT/CRIRES+ ($R_\lambda \sim 100\,000$; Kaeufl et al. 2004), Keck/KPIC ($R_\lambda \sim 35\,000$; Mawet et al. 2017), VLT/HiRISE ($R_\lambda \sim 100\,000$; Vigan et al. 2022), and Subaru/REACH ($R_\lambda \sim 100\,000$; Kotani et al. 2020). More recently, JWST has enriched this instrumental landscape from space by offering a combination of integral field spectroscopy and medium spectral resolution up to 28 μm with its instruments NIRSpec ($R_\lambda \sim 2700$; Böker et al. 2022) and MIRI ($R_\lambda \sim 3500$; Wells et al. 2015) that can image companions at a large separation (>100 mas). Naturally, the spectroscopic information contained in these data is exploited to characterize the atmosphere and the dynamic properties of the observed sources, with the spectral resolution guiding the type of parameters accessible.

With low-resolution spectra coupled with photometric data, it has been possible to estimate the effective temperature, T_{eff}, and surface gravity, log(g), of observed objects by analyzing the modified blackbody spectrum with significant water absorptions

★ Based on observations collected at the European Organization for Astronomical Research in the Southern Hemisphere under ESO programs 0101.C-0290; 0102.C-0121; 0103.C-0231; 0104.C-0094; 111.24PX.001; and 114.27B1.001.

★★ Corresponding author: `simon.petrus.pro@gmail.com`

★★★ NASA Postdoctoral Program Fellow.

★★★★ NASA Sagan Fellow.

(e.g., 51 Eri b Macintosh et al. 2015; HD 95086 b Desgrange et al. 2022; AF Lep b Palma-Bifani et al. 2024). Medium resolution has enabled the detection of molecules and atoms, enabling the estimation of relative chemical compositions such as the metallicity, [M/H], and carbon–oxygen ratio, C/O, (e.g., HR 8799 c Konopacky et al. 2013; VHS 1256 b Hoch et al. 2022; HIP 65426 b Petrus et al. 2021; AB Pic b Palma-Bifani et al. 2023) and isotopic ratios (e.g., TYC 8998-760-1 b Zhang et al. 2021a). Finally, the high resolution provides access to the vertical structure of planetary atmospheres as well as dynamic properties of companions, such as projected rotational velocity, v sin(i), and radial velocity (e.g., β Pic b Snellen et al. 2014; system HR 8799 Wang et al. 2021).

Estimating these atmospheric properties is now a critical challenge in exoplanetary science because they are potentially linked to the formation and evolution mechanisms of planetary systems. The [M/H] of atmospheres is considered a possible tracer of the amount of solid material accreted during formation (Ormel et al. 2021), while the C/O or the carbon monoxide isotopolog ratio, $^{13}CO/^{12}CO$, can provide insights into the formation distance of planets relative to their star, particularly relative to the location of the ice lines of key chemical elements such as H_2O, CO_2, and CO (Öberg et al. 2011). Although Mollière et al. (2022) highlight the interpretive limitations of these tracers, especially within the context of dynamic chemistry in disks, they remain crucial properties for constraining the structure and evolution of planetary atmospheres.

One approach used to constrain these properties is to compare the observed spectra of planetary companions with synthetic spectra generated from atmospheric model predictions. The current versions of the different families of models available allow for the generation of synthetic spectra at medium and high spectral resolutions over a wide wavelength coverage. Thus, it is possible to fit the observed data using their full potential, i.e., by maximizing both the spectral resolution and the wavelength range. However, due to the computational time required for such inversions, this method is mainly applicable using precompiled grids of synthetic spectra generated from self-consistent atmospheric models, which fix part of the physics and chemistry of the atmospheres with strong assumptions, limiting the number of explored parameters (fewer than 5) but reducing the computational time required for fitting. Indeed, with this approach, it is sufficient to interpolate within the grid, unlike retrieval methods that parametrize the physics and the chemistry of the atmospheres and calculate a new spectrum at each iteration based on the considered physics. Generally, reduced resolution spectra are used in this second case (Zhang et al. 2025, Matthews et al. 2025, Whiteford et al. 2025). The work presented here focuses on the use of precompiled grids.

Over the past 15 years, various grids of synthetic spectra have been developed and used. Each of these grids is generated by atmospheric models that differ in terms of complexity (cloud formation and evolution, nonequilibrium chemistry, micro-physics, initial chemical abundances, etc.), the parameter space explored, and wavelength coverage and resolution. A description of this diversity of models is detailed in Petrus et al. (2024), who used them to fit medium-resolution spectra of the companion VHS 1256 b (L7) obtained with JWST/NIRSpec and JWST/MIRI (Miles et al. 2023). In this study, Petrus et al. (2024) used the code `ForMoSA` (Petrus et al. 2020, 2023) to demonstrate the limitations of these models by showing that they failed to represent data over an extended wavelength range. One of the main reasons cited to explain these systematic errors is the complexity of the cloud properties present in the atmosphere of this object. To account for these systematic errors, they proposed a fitting strategy based on the definition of reduced spectral windows, fit independently. Although this technique significantly improves the quality of the fits, the robust estimation of C/O and [M/H] remains challenging. Indeed, the estimation of parameters depends on the spectral window as well as on the model considered. While the results of this work confirm the conclusions of previous studies using self-consistent atmospheric models (Petrus et al. 2020; Palma-Bifani et al. 2023), they are only valid for VHS 1256 b, known to be subject to significant photometric variability (Bowler et al. 2020; Zhou et al. 2020, 2022), likely due to a complex atmospheric structure and inhomogeneous cloud coverage, as is expected for an object at the L–T transition (Burgasser et al. 2002b; Cushing et al. 2008; Marley et al. 2010). The impact of these systematic errors on other spectral type ranges remains to be explored.

Today, the number of exoplanetary companions for which we have medium-resolution spectra over an extended wavelength range is limited due to the glare of their host stars. This prevents a homogeneous atmospheric characterization study over a wide temperature range. However, this diversity can be found in the population of young, isolated, low-mass brown dwarfs. Young, nearby associations have been identified as containing isolated very low-mass stars, substellar objects, and planetary mass objects. Some members of these associations overlap in spectral type, effective temperature, age, and mass with currently known directly imaged exoplanets. These similar physical properties are expected to imply similar atmospheric properties, and therefore this population of young isolated planetary-mass objects constitutes an ideal laboratory in which to explore physical processes at play in the atmospheres of imaged exoplanets.

However, for these isolated objects, a star-like formation through the gravitational collapse of molecular clouds is a plausible scenario. Therefore, despite their similarities with exoplanets, subtle differences in their atmospheric chemical compositions are expected. Consequently, characterizing their atmospheres offers a valuable point of comparison for exploring alternative formation pathways proposed for exoplanets, such as core accretion and gravitational instability.

Important efforts have been devoted to acquiring medium- and high-resolution spectra of these objects without a host star in a wide range of spectral types (early-M to late-L) and a large wavelength coverage (0.5–2.5 μm), to form libraries of planetary analog spectra (Bonnefoy et al. 2014; Gagné et al. 2015a; Cruz et al. 2018; Almendros-Abad et al. 2022; Hurt et al. 2024). These data can be used as comparison tools for the spectra of imaged companions (Samland et al. 2017; Chauvin et al. 2017; Mesa et al. 2023) to estimate their spectral type, among other things. They also serve as a database for conducting empirical analyses (Allers & Liu 2013; Filippazzo et al. 2015; Piscarreta et al. 2024), primarily based on the calculation of spectral indices or equivalent widths (EWs) of detected atomic and molecular absorptions. Furthermore, they can act as templates for generating simulated data used in the development of new instruments. Being devoid of a host star, it is also easier to obtain their mid-infrared spectra using space telescopes such as Spitzer or, now, JWST (Suárez & Metchev 2022).

In this article, we present the X-SHYNE[1] library, which comprises 43 spectra of brown dwarfs that have been selected to cover a large range of ages (<500 Myr), masses (<20 M_{Jup}), and T_{eff} (600-2000 K), overlapping the fundamental properties of the known imaged companions. X-SHYNE is therefore a

[1] X-Shooter spectra of YouNg Exoplanet analogs.

library of exoplanet analogs. The data have been obtained with the VLT/X-Shooter instrument to explore an extended wavelength range (0.3–2.5 μm) at medium resolutions ($R_\lambda \sim 8000$). This unique library allows one to probe the information carried by the pseudo-continuum sculpted by effective temperature, clouds, and H_2–H_2 and H_2–He collision-induced absorption (CIA). Additionally, the medium-resolution information can be exploited to estimate chemical composition and thus formation tracers. A first showcase publication targeted VHS 1256 b to illustrate the richness of the X-SHYNE library and prepare the analysis of Early Release Science data of JWST on this object (Petrus et al. 2023). With this work, we now analyze the complete X-SHYNE library, with three different grids of atmospheric models to characterize their atmospheres and identify the current limits of the models. Section 2 presents the sample of spectra. Section 3 is devoted to our empirical and homogeneous analysis of this library. Section 4 presents the inversion of our spectra using the three grids of models considered. A discussion of the results is made in Section 6, followed by a general conclusion in Section 7.

2. Observations and reduced spectra

The spectra were observed between April 28, 2018, and June 6, 2023, during six different observation periods. The VLT/X-Shooter instrument (Vernet et al. 2011) was used to obtain medium-resolution spectra ($R_{\lambda\ UVB} \sim 3300$ for $\lambda \in [0.3–0.55]$ μm, $R_{\lambda\ VIS} \sim 6700$ for $\lambda \in [0.55–0.1]$ μm, $R_{\lambda\ NIR} \sim 8100$ for $\lambda \in [0.1–2.5]$ μm) over a wide wavelength coverage (0.3–2.5μm). The observation dates and the weather conditions during the acquisition are detailed in Table A.1. The data were reduced using the X-Shooter pipeline version 2.9.3 (Modigliani et al. 2010) within the ESO `reflex` environment (Freudling et al. 2013) to obtain two-dimensional, curvature-corrected, and flux-calibrated traces. The spectrum extraction from these traces was performed with a custom extraction routine (see Petrus et al. 2023 for more details) coupled with the `molecfit` package (Smette et al. 2015; Kausch et al. 2015) for telluric correction.

Figure 1 shows an overview of the X-SHYNE spectral library after the extraction. As illustrated in the Figures B.1, B.2, B.3, B.4, and B.5, a huge diversity of atomic and molecular absorptions can be detected. Thanks to the large range of spectral types explored by X-SHYNE, it is possible to follow the evolution of these features with $T_{\rm eff}$. In the optical, the TiO (~0.69, 0.73, 0.77, 0.84, 0.90, 1.10 μm) and the VO (~0.75, 0.80, 1.07 μm) condensate progressively into solid grains and disappear around the L5 type. This depletion results in an increase in the absorption depth of other elements such as Rb I (0.795 and 0.780 μm) and Cs I (0.894 and 0.852 μm). For some of our targets, we detect a faint Li I absorption (0.671 μm), and for 2MASS 0249 c and 2MASS 0045, we detect an H_α emission line. In the near-infrared, the main atomic features are the K I doublets (1.177 and 1.169 μm and 1.252 and 1.243 μm) which become deeper with decreasing $T_{\rm eff}$, and the Na I doublet (1.140 and 1.138 μm) which disappears after the L-T transition. We also detect FeH (0.995 μm) and small traces of CrH (0.8611 μm). The H-band is sculpted by large absorption bands of H_2O. Due to the young age of our targets, this band displays a typical triangular shape (Lucas et al. 2001), which is completely remodeled after the L–T transition with the appearance of strong absorption bands of CH_4 long-ward of 1.59 μm. Lastly, in the K-band, numerous CO overtones are detected from 2.9 to 2.4 μm, along with a strong absorption band of CH_4 after the L-T transition.

3. Semiempirical analysis of the physical properties

By definition, because they have substellar masses, brown dwarfs cannot trigger hydrogen fusion in their cores. This lack of internal energy production leads to cooling over time due to radiative losses. Evolutionary models, such as `COND03` (Baraffe et al. 2003), predict how the fundamental properties of brown dwarfs evolve as a result of this cooling. For instance, the object contracts over time, leading to a decrease in radius. Since mass is assumed to remain constant with age, this contraction results in an increase in surface gravity. As a direct consequence of the decrease in $T_{\rm eff}$ and radius, the bolometric luminosity ($L_{\rm bol}$) also decreases with age, following the Stefan-Boltzmann law.

In this section, we estimate the age and $L_{\rm bol}$ of the X-SHYNE objects and inject these values into the `COND03` evolutionary model to derive other fundamental parameters. We first discuss the spectral types of our sample that are also strongly related to the $T_{\rm eff}$.

3.1. A wide range of spectral types covered

More than two decades ago, the empirical exploration of the morphology of brown dwarf spectra has led to the definition of the L (Kirkpatrick et al. 1999; Martín et al. 1999) and T (Burgasser et al. 2002a; Geballe et al. 2002) sequences. It was observed that with decreasing temperature, certain absorptions evolved, as did the overall shape of the pseudo-continuum (see Figures 1, B.1-B.5). These classifications have enabled the identification of template spectra libraries used to determine the spectral type of newly discovered objects. However, this method has its limitations. Cruz et al. (2018) demonstrated the differences that can exist between the spectral type determined from atomic (Cs, Rb) and molecular (VO, TiO, CrH, FeH) absorptions detected in the visible range (~0.6–0.9 μm) and the spectral type determined from near-infrared data (~1.0–2.5 μm), which are dominated by the effects of gravity, metallicity, and clouds condensation. Due to biases in the spectral type determination method and to remain conservative, we decided to assign an uncertainty of one spectral subclass to the spectral types of the X-SHYNE objects listed in Table 1. As a result, X-SHYNE covers a range of spectral types from L0±1 to T7±1.

3.2. Age determination

Stellar associations are ideal environments for the search and the characterization of low-mass brown dwarfs as the objects are comparatively brighter than those found in star-forming regions (Lucas et al. 2001; Lodieu et al. 2018; McCaughrean & Pearson 2023). Objects within these groups are assumed to share similar kinematic properties and age, under the hypothesis that they formed simultaneously in the same region. Age determination, in particular, currently relies on several diagnostics (see Gagné 2024 for a recent review). These include predictions from stellar and substellar internal structure models, often represented in color-magnitude diagrams (photometric isochrones, Nordström et al. 2004); measurements of stellar and substellar rotation for a given spectral type (gyro-chronology, Barnes 2009; Mamajek 2009); spectroscopic indicators of chromospheric activity or accretion, such as the H_α emission line; the presence of elements that are destroyed over time (e.g., lithium, Michaud & Charbonneau 1991; Rebolo 1991); X-ray activity; and the detection of infrared excess (Skumanich 1972; Soderblom et al. 1991).

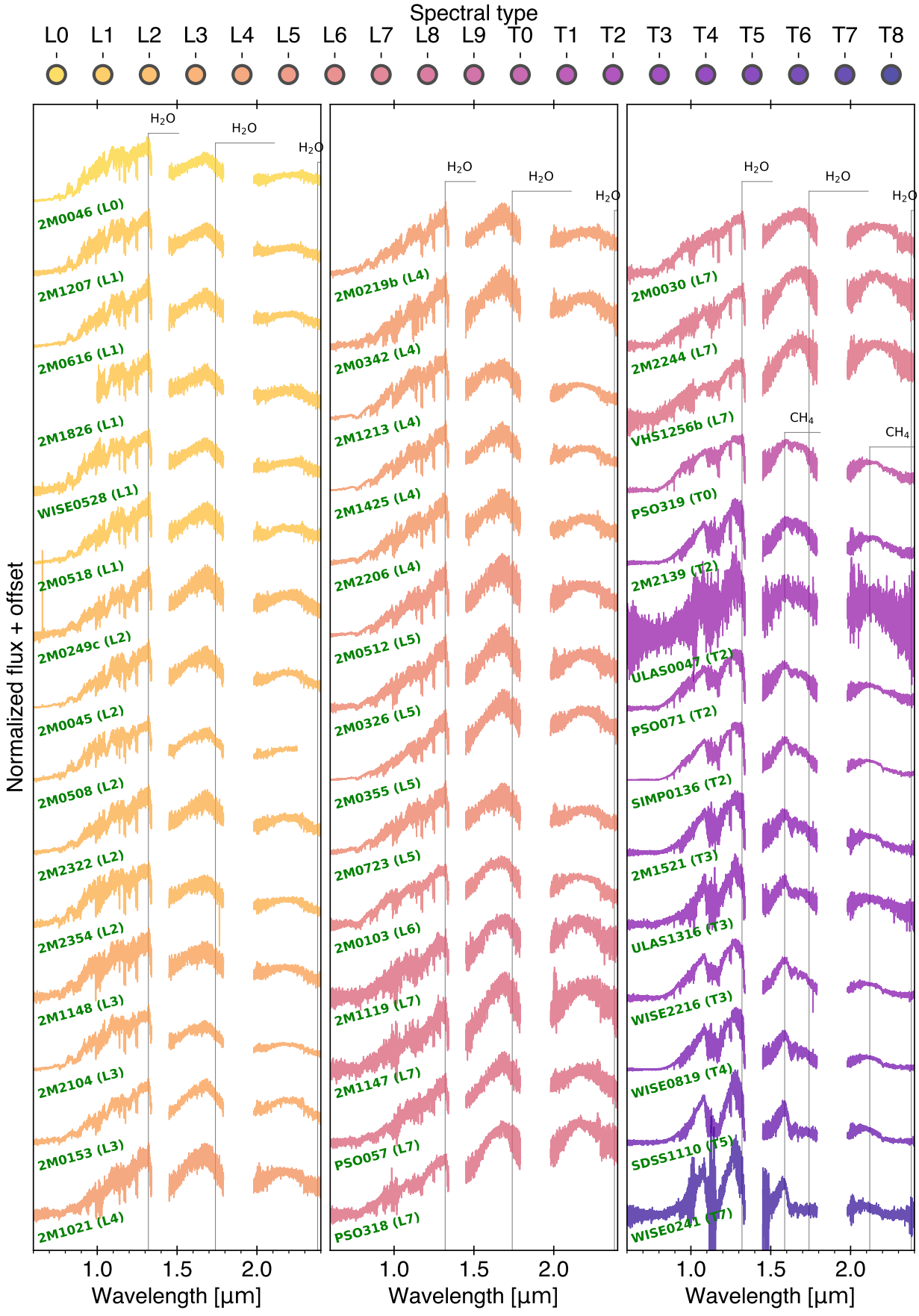

Fig. 1. Sequence of the X-SHYNE spectra. The integrated flux between 1.2 and 1.3 μm normalized the spectra, and an offset was applied. The color of each spectrum indicates its spectral type. Several zooms are given in Figures B.1, B.2, B.3, B.4, and B.5.

Table 1. X-SHYNE sample.

Target Simbad	Short	RA (hh:mm:ss.ss)	Dec (dd:mm:ss.ss)	Sp.T.	Assoc. (Memb. Prob.)	Dist. [pc]	Ref.
2MASSW J0030300-145033	2MASS 0030	00:30:30.13	–14:50:33.40	L7	Non-YMGM	24.3 ± 3.6^p	1, 2
2MASS J00452143+1634446	2MASS 0045	00:45:21.42	+16:34:44.74	L2	ARG (99.3%)	15.3 ± 0.1^p	3, 4
2MASS J00464841+0715177	2MASS 0046	00:46:48.42	+07:15:17.76	L0	Non-YMGM	37.7 ± 0.4^p	3, 4
2MASSI J0103320+193536	2MASS 0103	01:03:32.04	+19:35:36.18	L6	CRIUS203 (99.6%)	27.8 ± 5.2^p	1, 5
2MASS J01531463-6744181	2MASS 0153	01:53:14.63	–67:44:18.20	L3	Tuc-Hor (91.4%)	47.0 ± 3.2	6
2MASS J02192210-3925225b	2MASS 0219 b	02:19:22.11	–39:25:22.54	L4	Tuc-Hor (99.7%)	40.2 ± 0.2^p	7, 4
2MASS J02495436-0558015	2MASS 0249 c	02:49:54.37	–05:58:01.58	L2	Non-YMGM	49.8 ± 10.5^p	8
2MASS J03264225-2102057	2MASS 0326	03:26:42.26	–21:02:05.77	L5	ABDMG (95.6%)	41 ± 4	9, 10
2MASSI J0342162-681732	2MASS 0342	03:42:16.21	–68:17:32.12	L4	Tuc-Hor (95.0%)	81 ± 1	11, 10
2MASS J03552337+1133437	2MASS 0355	03:55:23.37	+11:33:43.80	L5	ABDMG (97.8%)	9.2 ± 0.1^p	12, 4
2MASS J05081657-1413479	2MASS 0508	05:08:16.58	–14:13:48.04	L2	ABDMG (98.6%)	42.6 ± 1.1^p	13, 4
2MASSI J0512063-294954	2MASS 0512	05:12:06.37	–29:49:54.01	L5	Non-YMGM	20.2 ± 1.2^p	14, 15
2MASSI J0518461-275645	2MASS 0518	05:18:46.17	–27:56:45.71	L1	COL (99.9%)	54.6 ± 1.9^p	11, 4
2MASS J06165623-2543557	2MASS 0616	06:16:56.23	–25:43:55.75	L1	Non-YMGM	50.3 ± 24.4^p	16, 17
2MASS J07235265-3309446	2MASS 0723	07:23:52.66	–33:09:44.54	L5	CARN (99.6%)	32.5 ± 2.3^p	18, 4
2MASS J10212570-2830427	2MASS 1021	10:21:25.71	–28:30:42.76	L4	Non-YMGM	43.4 ± 6.4	6, 19
TWA 42	2MASS 1119	11:19:32.54	–11:37:46.70	L7	Non-YMGM	26.6 ± 6.9	20, 21
TWA 41	2MASS 1147	11:47:24.21	–20:40:20.44	L7	Non-YMGM	37.5 ± 3.0^p	22, 2
2MASS J11480096-2836488	2MASS 1148	11:48:00.96	–28:36:48.90	L3	Non-YMGM	47.8 ± 5.6	6
TWA 40	2MASS 1207	12:07:48.35	–39:00:04.48	L1	TWA (98.0%)	65.6 ± 4.4^p	23, 4
2MASS J12130336-0432437	2MASS 1213	12:13:03.34	–04:32:43.75	L4	CARN (99.3%)	16.9 ± 0.2^p	14, 4
2MASS J14252798-3650229	2MASS 1425	14:25:27.98	–36:50:23.25	L4	ABDMG (99.1%)	11.8 ± 0.1^p	24, 4
2MASS J15210327+0131426	2MASS 1521	15:21:03.27	+01:31:42.69	T3	Non-YMGM	23.1 ± 3.9^p	25, 2
2MASS J18264679-4602234	2MASS 1826	18:26:46.80	–46:02:23.64	L1	BPMG (96.0%)	58.1 ± 7.2^p	13, 4
2MASS J21043128-0939217	2MASS 2104	21:04:31.29	–09:39:21.82	L3	BPMG (83.5%)	53.5 ± 5.0^p	13, 4
CFBDS J213926+022023	2MASS 2139	21:39:26.77	+02:20:22.70	T2	CRIUS203 (96.6%)	9.9 ± 0.2^p	26, 27
2MASSW J2206450-421721	2MASS 2206	22:06:45.00	–42:17:21.14	L4	ABDMG (99.5%)	29.3 ± 1.2^p	1, 4
2MASS J22443167+2043433	2MASS 2244	22:44:31.67	+20:43:43.30	L7	ABDMG (98.4%)	17.0 ± 0.3^p	9, 28
2MASS J23225299-6151275	2MASS 2322	23:22:53.01	–61:51:27.53	L2	Tuc-Hor (96.0%)	42.9 ± 1.9^p	29, 4
PSO J358.5527+22.1393	2MASS 2354	23:54:12.57	+22:08:22.58	L2	ABDMG (99.0%)	43.5 ± 1.2^p	30, 4
PSO J057.2893+15.2433	PSO 057	03:49:09.44	+15:14:36.00	L7	Non-YMGM	25.2 ± 3.0	31
2MASS J04473039-1216155	PSO 071	04:47:30.40	–12:16:15.54	T2	Non-YMGM	43.5 ± 8.9^p	31, 2
2MASS J21140802-2251358	PSO 318	21:14:08.03	–22:51:35.84	L7	BPMG (99.0%)	22.2 ± 0.9^p	32, 28
2MASS J21171431-2940034	PSO 319	21:17:14.31	–29:40:03.42	T0	Non-YMGM	19.1 ± 2.8^p	31, 2
2MASS J11101001+0116130	SDSS 1110	11:10:10.01	+01:16:13.09	T5	ABDMG (87.4%)	19.2 ± 0.5^p	33, 34
SIMP J013656.5+093347.3	SIMP 0136	01:36:56.56	+09:33:47.31	T2	CARN (96.3%)	6.1 ± 0.1^p	35, 4
ULAS J004757.40+154641.4	ULAS 0047	00:47:57.32	+15:46:41.56	T2	non-YMGM	37.0 ± 4.5^p	36, 37
ULAS J131610.13+031205.5	ULAS 1316	13:16:10.13	+03:12:05.56	T3	CARN (95.9%)	34.5 ± 3.1^p	38, 2
SIPS J1256-1257B	VHS 1256 b	12:56:01.83	–12:57:27.69	L7	Non-YMGM	22.2 ± 1.3^p	39, 40
WISE J024124.73-365328.0	WISE 0241	02:41:24.74	–36:53:28.09	T7	ARG (91.5%)	19.1 ± 1.0^p	41, 5
WISE J052857.68+090104.4	WISE 0528	05:28:57.69	+09:01:04.40	L1	Non-YMGM	81 ± 13	42
2MASS J08195820-0335266	WISE 0819	08:19:58.21	–03:35:26.65	T4	BPMG (83.9%)	13.9 ± 0.6^p	43, 2
PSO J334.1193+19.8800	WISE 2216	22:16:28.62	+19:52:48.10	T3	Non-YMGM	30.0 ± 11.2	31

Notes. ^{p}: Distance calculated from parallax measurements. 1. Kirkpatrick et al. (2000); 2. Best et al. (2020); 3. Wilson et al. (2003); 4. Gaia Collaboration (2020); 5. Kirkpatrick et al. (2021); 6. Gagné et al. (2015b); 7. Artigau et al. (2015); 8. Dupuy et al. (2018); 9. Dahn et al. (2002); 10. Faherty et al. (2009); 11. Cruz et al. (2007); 12. Reid et al. (2006); 13. Gagné & Faherty (2018); 14. Cruz et al. (2003); 15. Best et al. (2021); 16. Cushing et al. (2009); 17. Faherty et al. (2012); 18. Schneider et al. (2017); 19. Gagné et al. (2017); 20. Kellogg et al. (2015); 21. Best et al. (2017); 22. Faherty et al. (2016); 23. Gagné et al. (2014); 24. Kendall et al. (2004); 25. Knapp et al. (2004); 26. Burgasser et al. (2006); 27. Smart et al. (2013); 28. Liu et al. (2016); 29. Reid et al. (2008); 30. Aller et al. (2016); 31. Best et al. (2015); 32. Liu et al. (2013); 33. Geballe et al. (2002); 34. Tinney et al. (2014); 35. Artigau et al. (2006); 36. Day-Jones et al. (2013); 37. Zhang et al. (2021b); 38. Marocco et al. (2015); 39. Gauza et al. (2015); 40. Dupuy et al. (2020); 41. Tinney et al. (2018); 42. Burgasser et al. (2016); 43. Kirkpatrick et al. (2011).

Most of the X-SHYNE objects were selected as Young co-Moving Group Members (YMGM) or member candidates before the important Gaia DR2 release that significantly modified key kinematics properties for these objects. The properties of the groups considered in this work are summarized in Table 2. Using updated astrometry and radial velocity measurements, we recalculated the membership probability for each X-SHYNE target with the `BANYAN Σ` tool (Gagné et al. 2018). These results, along with their associated probabilities, are summarized in Table 1. For objects with a membership probability below 80%, we classified them as Non-Young co-Moving Group Members (non-YMGM). Consequently, their age remains uncertain and

Table 2. Properties of the young associations considered in this work.

Name	Distance (pc)	Age (Myr)	$N_{X-SHYNE}$	Ref.
ABDMG	~20	149^{+19}_{-51}	8	1, 2
ARG	~140	~40	2	2, 3
BPMG	~35	24±3	4	2, 4
CARN	~30	~200	4	5
COL	~70	42^{+6}_{-4}	1	2, 6
CRIUS203	–	~500	2	6, Priv. com.
Tuc-Hor	~50	45±4	4	2, 6
TWA	~65	10±3	1	2, 6
non-YMGM	–	–	17	–

Notes. The number of X-SHYNE objects associated with each group is given. 17 sources are not identified as members of a young moving group (non-YMGM). Full names: AB Doradus, ABDMG; Argus, ARG; β Pictoris, BPMG; Carina-Near, CARN; Columba, COL; Tucana Horologium, Tuc-Hor; TW Hydrae, TWA. 1. Zuckerman et al. (2004); 2. Bell et al. (2015); 3. Torres et al. (2008); 4. Zuckerman et al. (2001); 5. Zuckerman et al. (2006); 6. Moranta et al. (2022).

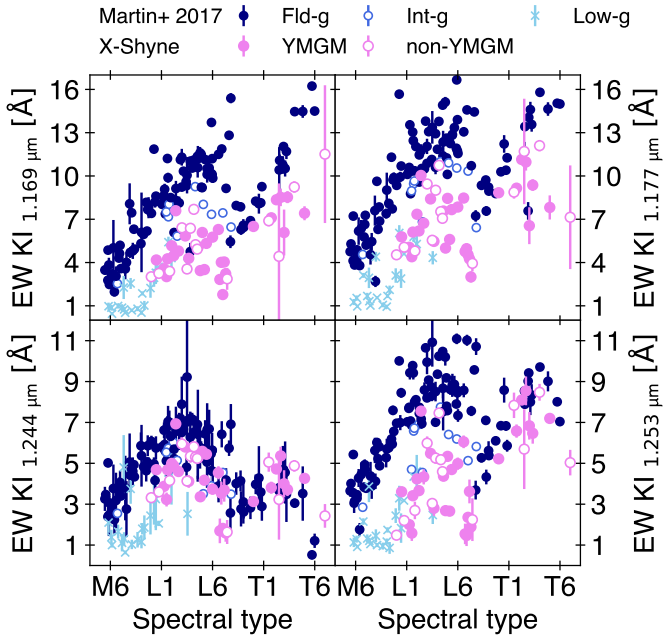

Fig. 2. Equivalent widths (EW) of the four potassium absorption lines detected at 1.169, 1.177, 1.244, and 1.253 μm. To confirm the young age of X-SHYNE's objects, we compared their EWs (pink) with the EW calculated for the low, intermediate, and field gravity objects from the library of spectra published by Martin et al. (2017) (blue). To improve the clarity of the plot, objects that share the same spectral type have been evenly distributed within a range corresponding to their spectral type ±1.

requires further confirmation. In the specific case of the companion VHS 1256 b, although it is classified as a non-YMGM, the age of its primary star has been derived independently by Dupuy et al. (2023) as 140±20 Myr and will be assumed as the age of the companion.

The EW of the potassium lines at 1.169, 1.177, 1.244, and 1.253 μm are known to be robust discriminants between old and young L- and M-type objects (Cushing et al. 2005; Bayo et al. 2011; Allers & Liu 2013; Bonnefoy et al. 2014; Martin et al. 2017; Manjavacas et al. 2020; Piscarreta et al. 2024). This is because their strength correlates with the pressure in the photosphere, which, in turn, is linked to the surface gravity of the object. The K I EW of some X-SHYNE objects has previously been calculated and analyzed in Piscarreta et al. (2024). To ensure the homogeneity of our study, we recalculated these values using our framework.

To achieve this, we estimated the pseudo-continuum on both sides of the spectral line by calculating the median flux within the spectral ranges $d\lambda_{\rm cont.left}$ and $d\lambda_{\rm cont.right}$, as listed in Table 4. We then linearly interpolated these two flux values across the spectral range, $d\lambda_{\rm line}$, defined for the line. Finally, we computed the EW using the following equation:

$$EW = \sum_{\lambda} \left(1 - \frac{F_{line}}{F_{cont.interp}}\right) \times d\lambda, \quad (1)$$

where F_{line} and $F_{cont.interp}$ represent the flux values of the spectral line and the interpolated pseudo-continuum, respectively, at the location of the line. The term $d\lambda$ corresponds to the wavelength grid of the data.

We then compared the EW of the four K I absorption lines in the X-SHYNE sources with those derived from the spectral library (R_λ ~2000) published by Martin et al. (2017). This library includes isolated brown dwarfs with low, medium, and high surface gravity, corresponding to young (<30 Myr), intermediate (30–100 Myr), and field (>100 Myr) ages, respectively. In their study, Martin et al. (2017) calculated the EW following the method described by Allers & Liu (2013), which determines the pseudo-continuum at each line location using a linear interpolation between two spectral windows located on either side of the line. To ensure a consistent comparison, we adopted the same technique. To estimate the error bars, we followed the procedure described in Petrus et al. (2023). Specifically, for each target, we constructed 100 spectra by randomly generating the flux at each wavelength using a Gaussian distribution, with the mean set to the initial flux value and the standard deviation equal to the flux error. The final EW value and its associated error were obtained as the mean and standard deviation of the 100 EWs, respectively.

Figure 2 shows the evolution of the four EWs as a function of spectral type. We confirmed that the EWs measured for young objects are significantly lower than those of field objects for L-type dwarfs. This trend persists for T-dwarfs with the K I lines at 1.169 and 1.177 μm, but is less clear for the K I lines at 1.243 and 1.253 μm, which are blended with a FeH feature that can affect the EW measurement. Manjavacas et al. (2020) and Martin et al. (2017) established empirical relations between these EWs and the ages of objects at the M/L transition. These relations do not enable a reliable age estimation for the non-YMGM objects in X-SHYNE, which spans the L/T transition. Furthermore, our sample size is too limited to derive such relationships independently in that work. However, we confirm the young age of all X-SHYNE objects (10–500 Myr).

3.3. Bolometric luminosity determination

The calculation of L_{bol} is not straightforward because it requires integrating the emitted flux of an object over its entire spectral energy distribution (SED), while available data often only cover a fraction of this SED. Atmospheric models are typically used to fill these wavelength gaps (e.g., Stephens et al. 2009; Dieterich et al. 2014; Carter et al. 2023), but their systematic errors, along

Table 3. Properties of the X-SHYNE library from the semiempirical analysis.

Target	log(L/L$_\odot$)	Mass (M$_{Jup}$)	T$_{eff}$ (K)	Radius (R$_{Jup}$)	log(g) (dex)
2MASS 0030	–4.44 ± 0.21	–	–	–	–
2MASS 0045	–3.63 ± 0.06	$19.1^{+0.96}_{-4.96}$	1885^{+18}_{-90}	$1.49^{+0.08}_{-0.11}$	$4.35^{+0.08}_{-0.15}$
2MASS 0046	–3.26 ± 0.06	–	–	–	–
2MASS 0103	–4.2 ± 0.24	$44.01^{+10.43}_{-10.22}$	1641^{+247}_{-221}	$1.0^{+0.05}_{-0.0}$	$5.06^{+0.09}_{-0.15}$
2MASS 0153	–3.89 ± 0.11	$14.19^{+3.53}_{-2.0}$	1647^{+122}_{-95}	$1.42^{+0.06}_{-0.05}$	$4.25^{+0.11}_{-0.05}$
2MASS 0219 b	–3.84 ± 0.21	$15.09^{+5.59}_{-3.13}$	1691^{+217}_{-173}	$1.43^{+0.11}_{-0.07}$	$4.27^{+0.16}_{-0.07}$
2MASS 0249 c	–3.99 ± 0.28	–	–	–	–
2MASS 0326	–3.8 ± 0.15	$32.53^{+8.81}_{-8.06}$	1887^{+169}_{-173}	$1.2^{+0.06}_{-0.03}$	$4.77^{+0.1}_{-0.15}$
2MASS 0342	–3.51 ± 0.11	$15.83^{+8.99}_{-1.15}$	1941^{+168}_{-92}	$1.57^{+0.07}_{-0.16}$	$4.22^{+0.21}_{-0.02}$
2MASS 0355	–4.13 ± 0.05	$24.51^{+3.93}_{-6.62}$	1582^{+72}_{-98}	$1.18^{+0.05}_{-0.02}$	$4.65^{+0.08}_{-0.17}$
2MASS 0508	–3.68 ± 0.07	$36.68^{+6.35}_{-7.58}$	2006^{+93}_{-109}	$1.22^{+0.05}_{-0.03}$	$4.8^{+0.08}_{-0.12}$
2MASS 0512	–4.15 ± 0.11	–	–	–	–
2MASS 0518	–3.42 ± 0.09	$22.19^{+5.68}_{-7.13}$	2051^{+134}_{-120}	$1.62^{+0.13}_{-0.08}$	$4.36^{+0.12}_{-0.18}$
2MASS 0616	–3.52 ± 0.64	–	–	–	–
2MASS 0723	–3.92 ± 0.13	$32.41^{+5.72}_{-4.24}$	1798^{+132}_{-121}	$1.17^{+0.02}_{-0.02}$	$4.79^{+0.06}_{-0.07}$
2MASS 1021	–4.14 ± 0.24	–	–	–	–
2MASS 1119	–4.41 ± 0.36	–	–	–	–
2MASS 1147	–4.21 ± 0.14	–	–	–	–
2MASS 1148	–3.89 ± 0.19	–	–	–	–
2MASS 1207	–3.39 ± 0.13	$13.38^{+1.4}_{-3.12}$	1985^{+98}_{-131}	$1.71^{+0.13}_{-0.08}$	$4.07^{+0.02}_{-0.11}$
2MASS 1213	–4.17 ± 0.07	$26.31^{+2.72}_{-2.75}$	1573^{+71}_{-75}	$1.16^{+0.01}_{-0.01}$	$4.7^{+0.05}_{-0.05}$
2MASS 1425	–4.04 ± 0.05	$26.67^{+3.9}_{-5.71}$	1667^{+69}_{-92}	$1.19^{+0.04}_{-0.02}$	$4.69^{+0.08}_{-0.12}$
2MASS 1521	–4.75 ± 0.31	–	–	–	–
2MASS 1826	–3.76 ± 0.21	$12.11^{+1.81}_{-1.81}$	1723^{+160}_{-162}	$1.53^{+0.09}_{-0.06}$	$4.13^{+0.01}_{-0.04}$
2MASS 2104	–3.7 ± 0.15	$12.5^{+1.41}_{-1.32}$	1767^{+114}_{-114}	$1.54^{+0.08}_{-0.05}$	$4.14^{+0.01}_{-0.03}$
2MASS 2139	–4.76 ± 0.1	$28.82^{+3.21}_{-4.65}$	1182^{+73}_{-69}	$1.01^{+0.04}_{-0.01}$	$4.85^{+0.06}_{-0.11}$
2MASS 2206	–3.95 ± 0.09	$28.69^{+5.82}_{-6.61}$	1747^{+111}_{-128}	$1.19^{+0.05}_{-0.03}$	$4.72^{+0.09}_{-0.14}$
2MASS 2244	–4.51 ± 0.08	$12.61^{+7.96}_{-0.92}$	1234^{+120}_{-51}	$1.24^{+0.03}_{-0.09}$	$4.32^{+0.28}_{-0.04}$
2MASS 2322	–3.73 ± 0.09	$17.17^{+3.37}_{-3.9}$	1791^{+110}_{-103}	$1.46^{+0.08}_{-0.07}$	$4.31^{+0.11}_{-0.11}$
2MASS 2354	–3.74 ± 0.09	$34.7^{+6.88}_{-7.44}$	1949^{+113}_{-125}	$1.21^{+0.05}_{-0.03}$	$4.79^{+0.09}_{-0.13}$
PSO 057	–4.58 ± 0.18	–	–	–	–
PSO 071	–4.29 ± 0.31	–	–	–	–
PSO 318	–4.52 ± 0.09	$6.58^{+1.02}_{-0.91}$	1177^{+61}_{-59}	$1.39^{+0.02}_{-0.02}$	$3.94^{+0.06}_{-0.07}$
PSO 319	–4.46 ± 0.22	–	–	–	–
SDSS 1110	-5.01 ± 0.18	$11.63^{+0.32}_{-2.94}$	961^{+105}_{-116}	$1.18^{+0.03}_{-0.01}$	$4.33^{+-0.0}_{-0.14}$
SIMP 0136	–4.73 ± 0.27	$12.28^{+8.71}_{-1.1}$	1119^{+222}_{-152}	$1.21^{+-0.02}_{-0.07}$	$4.33^{+0.29}_{-0.02}$
ULAS 0047	–4.71 ± 0.31	–	–	–	–
ULAS 1316	–4.46 ± 0.25	$19.86^{+6.82}_{-7.7}$	1331^{+224}_{-205}	$1.16^{+0.06}_{-0.0}$	$4.58^{+0.13}_{-0.26}$
VHS 1256 b	–4.46 ± 0.55	$13.37^{+16.72}_{-2.38}$	1265^{+518}_{-320}	$1.24^{+-0.03}_{-0.05}$	$4.35^{+0.39}_{-0.04}$
WISE 0241	–5.3 ± 0.53	$4.82^{+4.07}_{-2.51}$	776^{+270}_{-204}	$1.27^{+0.04}_{-0.03}$	$3.88^{+0.28}_{-0.32}$
WISE 0528	–3.55 ± 0.22	–	–	–	–
WISE 0819	–4.79 ± 0.31	$5.04^{+2.26}_{-1.68}$	1019^{+191}_{-163}	$1.37^{+0.04}_{-0.03}$	$3.84^{+0.15}_{-0.16}$
WISE 2216	–4.75 ± 0.54	–	–	–	–

with the difficulty of propagating these uncertainties into the error bars of L$_{bol}$, may bias its calculation and interpretation. Bolometric corrections, which establish a relationship between L$_{bol}$ and specific photometric points, can also be employed (e.g., Golimowski et al. 2004; Vrba et al. 2004; Zapatero Osorio et al. 2014). However, similarly to atmospheric models, this method suffers from systematic errors and significant dispersion, particularly for late-L and T-type objects. To provide a more robust estimate of L$_{bol}$, Filippazzo et al. (2015) proposed a method that reconstructs the full SED by combining available spectroscopic and photometric data. For some X-SHYNE targets, this approach has already been applied by Filippazzo et al. (2015),

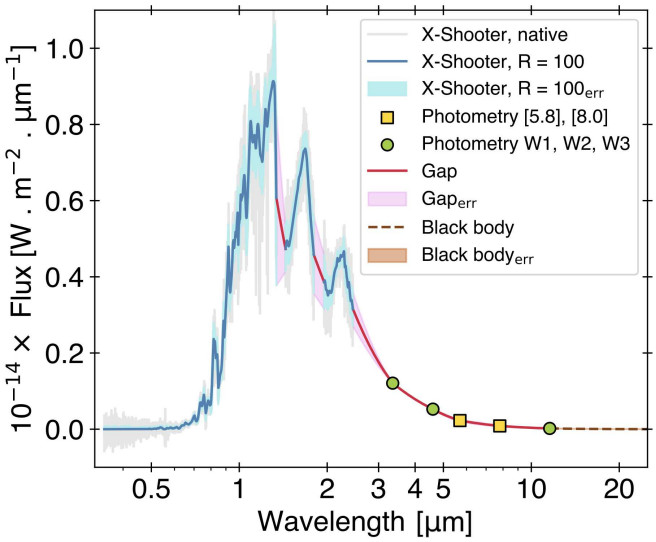

Fig. 3. Reconstruction of the SED. We have adapted the procedure described in Filippazzo et al. (2015) to combine our X-Shooter spectra with previously obtained photometric data. This reconstructed SED was used to calculate the bolometric luminosity of our targets. The example presented here is 2MASS 0046.

Table 4. Wavelength ranges used to calculate the EWs of each K I line.

K I lines (μm)	$d\lambda_{cont.left}$ (μm)	$d\lambda_{line}$ (μm)	$d\lambda_{cont.right}$ (μm)
1.169	1.155–1.167	1.168–1.1705	1.1705, 1.175
1.177	1.1708–1.1757	1.1757–1.179	1.180–1.185
1.244	1.235–1.2417	1.2417–1.2445	1.246–1.250
1.253	1.246–1.250	1.250–1.255	1.255–1.265

Faherty et al. (2016) and more recently by Sanghi et al. (2023a). By adding new spectra obtained from X-Shooter, we have decided to recalculate L_{bol} for every targets, homogeneously, following the same methodology. Figure 3 illustrates the various contributions to the L_{bol} calculation, using 2MASS 0046 (L0) as a case study.

3.3.1. Spectroscopic data

We used X-Shooter data covering the wavelength range between 0.345 and 2.45 μm. To calculate a robust value of L_{bol} and mitigate the noise that can affect high-resolution data, we focused on the pseudo-continuum by reducing the spectral resolution to R_λ ~100 by applying a Gaussian filter. The new error bars were estimated as the standard deviation of the native spectrum within a box of 1000 spectral channels centered around each point. To avoid contamination from the broad water absorption bands, we selected only three spectral regions: SHORT (0.345–1.340 μm), H (1.44–1.80 μm), and K (1.952–2.450 μm). Due to data quality issues, likely caused by slit misalignment during observations, the SHORT-band was restricted to 1.01–1.34 μm for 2MASS 1826 and to 0.6–1.34μm for ULAS 1316. Similarly, the K-band for 2MASS 0508 was limited to 1.952–2.22 μm.

3.3.2. Photometric data

We considered five different photometric points. The W1 ($\Delta\lambda$ = 2.754–3.872 μm), W2 ($\Delta\lambda$ = 3.963–5.341 μm), and W3 ($\Delta\lambda$ = 7.443–17.261 μm) values and their associated errors, were retrieved from Marocco et al. (2021) and Cutri & et al. (2012). For 2MASS 0219 b, SIMP 0136, VHS 1256 b, WISE 0241, and WISE 0819, for which WISE photometry was unavailable, we estimated the photometric values using the empirical relation between spectral type and WISE photometry defined by Faherty et al. (2016). The uncertainties were propagated by combining the error from the relation itself with an additional uncertainty of 1 spectral subtype.

In addition to the WISE data points, the IRAC [5.8 μm] and [8 μm] photometry were considered for reconstructing the SED. However, since these IRAC measurements were not available for most of our targets, we chose to estimate them using semiempirical relations between these two IRAC bands and WISE photometry, as was established by Filippazzo et al. (2015). This approach ensures a more robust estimate of the SED at these wavelengths compared to simple interpolation, as described in Section 3.3.3. These relations differ slightly between young and old objects and are only valid within a specific range of W1 magnitudes. We prioritized the relation defined for young objects; however, for WISE 0241 and WISE 0819, we used the relation for old objects because their W1 photometry fell outside the valid range for young-object relations. Nevertheless, since the flux values at these wavelengths are very low, this choice has only a minimal impact on the L_{bol} calculation. As before, the uncertainties were propagated by combining the error from the relation itself with the uncertainty associated with the considered W1 magnitude.

3.3.3. Gaps definition

To construct a complete SED covering the entire wavelength range, we filled the gaps between the different datasets. The water bands, as well as the gaps between photometric points, were filled using a linear interpolation of the logarithms of the fluxes on either side of the gaps. This approach mimics the behavior of a blackbody law at these wavelengths. We also fit a blackbody law to the photometric points and used it to extend the SED between the W3 photometric point and 1 mm. At wavelengths shorter than 0.360 μm, we assumed zero flux, since this spectral range – uncovered by X-Shooter – contributes less than 0.01% of the total flux, according to atmospheric models. For 2MASS 1826, an additional blackbody law was fit using the wavelength range between 1.000 and 1.345 μm to fill the SED between 0.36 and 1.00 μm. The flux gaps were computed for the mean data flux, as well as for the minimum and maximum data flux values, by propagating the applying uncertainties. This allowed us to define the errors at the locations of the gaps. To calculate the L_{bol} we integrated the spectroscopic data with the reduced resolution and the gaps between 0.346 and 1000 μm considering negative flux as null.

3.4. Masses, temperatures, and radii predicted by evolutionary models

For the YMGMs of X-SHYNE, we used our age estimates (defined in Section 3.2) and our L_{bol} estimates (defined in Section 3.3) as inputs into the `COND03` evolutionary model (Baraffe et al. 2003). We linearly interpolated this model to estimate the radius, mass, T_{eff}, and log g of the objects. The behavior of these parameters within the `COND03` model, as well as the predictions for the X-SHYNE sample, are illustrated in Figure 4. This semiempirical analysis confirms the impact of the T_{eff} on the spectral type as identified in many other studies (e.g., Kirkpatrick et al. 1999, Burgasser et al. 2002a). It also confirms that a young

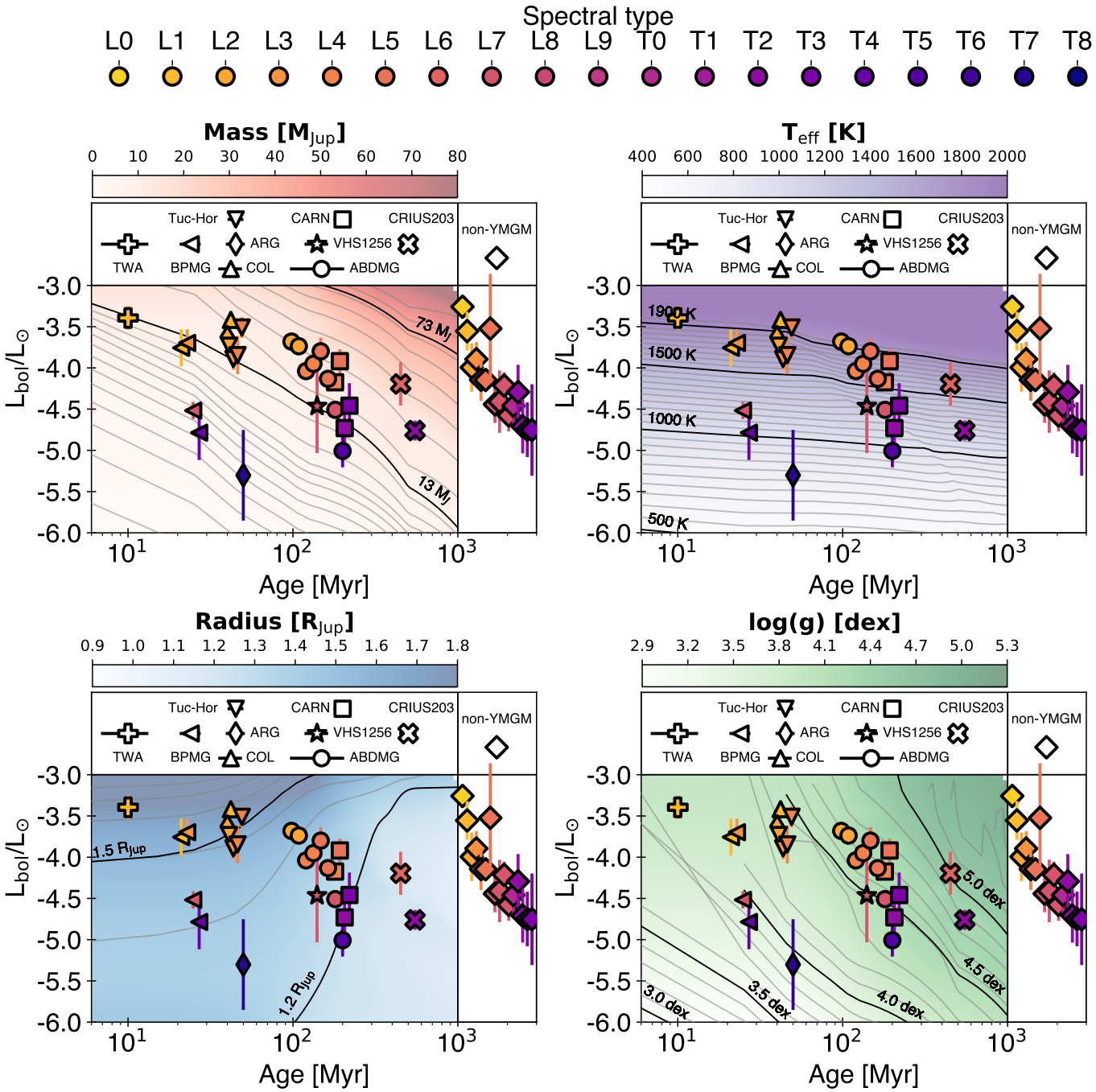

Fig. 4. Prediction of the evolutionary model COND03 (Baraffe et al. 2003). We injected the age estimated in Section 3.2 and the L_{bol} calculated in Section 3.3 into the model, which we interpolated linearly to estimate the mass (top-left panel, red background), T_{eff} (top-right panel, purple background), radius (bottom-left panel, blue background), and log(g) (bottom-right panel, green background). The non-YMGM objects, for which we do not have an age estimate, are plotted on the right side of each panel. For each parameter, we also display its variation as a function of L_{bol} and age (color bar and solid gray and black lines). The shape of each X-SHYNE dot represents its membership, while its color corresponds to its spectral type. To improve the clarity of the plot, objects that share the same age have been evenly distributed within a range corresponding to the error bars of that age.

early-L dwarf can have the same mass as an older T-type dwarf. Additionally, we notice that the predicted radii of old, low-mass objects, which are expected to reach values below 1 R_{Jup}, show significant dispersion. The luminosity, mass, T_{eff}, radius, and log(g) values for the X-SHYNE YMGMs estimated from this semiempirical analysis are summarized in Table 3. These results will be compared to the ones derived in the next section, which presents our synthetic analysis.

4. Synthetic atmosphere analysis

Recent work led by Petrus et al. (2020, 2023, 2024) and Palma-Bifani et al. (2023) has confirmed the results from Marocco et al. (2014) who showed the limitations of fitting models using wide wavelength coverages, demonstrating that atmospheric models fail to reproduce the data globally. Considering a diversity of models, they have highlighted the interest of independent fits by

Table 5. Priors used for the fits with the three synthetic spectra grids considered.

Param.		Exo-REM	Sonora	ATMO
T_{eff}	(K)	$\mathcal{U}(400, 2000)$	$\mathcal{U}(900, 2400)$	$\mathcal{U}(800, 3000)$
log(g)	(dex)	$\mathcal{U}(3.0, 5.0)$	$\mathcal{U}(3.5, 5.5)$	$\mathcal{U}(2.5, 5.5)$
[M/H]		$\mathcal{U}(-0.5, 0.5)$	$\mathcal{U}(-0.5, 0.5)$	$\mathcal{U}(-0.6, 0.6)$
C/O		$\mathcal{U}(0.1, 0.8)$	–	$\mathcal{U}(0.3, 0.7)$
f_{sed}		–	$\mathcal{U}(1.0, 8.0)$	–
γ		–	–	$\mathcal{U}(1.01, 1.05)$
RV	(km s^{-1})	$\mathcal{U}(-100, 100)$	$\mathcal{U}(-100, 100)$	$\mathcal{U}(-100, 100)$
R	(R_{Jup})	$\mathcal{U}(0, 10)$	$\mathcal{U}(0, 10)$	$\mathcal{U}(0, 10)$
d	(pc)	$\mathcal{N}(d_i,\ d^2_{err,i})$	$\mathcal{N}(d_i,\ d^2_{err,i})$	$\mathcal{N}(d_i,\ d^2_{err,i})$

Notes. d_i and $d^2_{err,i}$ are the distance and its error, respectively, given in Table 1.

selecting restricted wavelength windows that can be accurately reproduced by the models. In particular, Petrus et al. (2024) proposed a method to propagate part of the systematic errors of the models into the final parameter errors by exploiting the dispersion of these estimations for different spectral windows considered for the independent fits. However, this technique has its own limitations. It is still dependent of the quality of the models and their ability to reproduce correctly the spectral feature. For instance Petrus et al. (2024) noticed that in the case of VHS 1256 b, nonphysical parameters estimated at the location of a silicate absorption (∼10 µm) which was known to be not reproduced by the models, could bias the final results. Therefore, the results are dependent of the choice of the spectral windows considered. In this work, we propose another approach to take into account the systematic errors of the models.

4.1. The atmospheric models

In this study, we consider three different grids of synthetic spectra. The `Exo-REM` model (Charnay et al. 2018) incorporates nonequilibrium chemistry between CO, CH_4, CO_2, and NH_3, and the formation of clouds composed of iron, Na_2S, KCl, silicates, and water. The `Sonora-diamondback` model (hereafter `Sonora`) (Morley et al. 2024) assumes chemical equilibrium throughout the atmosphere and includes a cloud model parameterized by a sedimentation factor f_{sed}. The `ATMO` model (Tremblin et al. 2015) simulates the impact of clouds on the spectrum through diabatic convection (fingering convection) led by the adiabatic index γ generated by nonequilibrium chemical reactions: CO/CH_4 at the L-T transition and N_2/NH_3 at the T-Y transition. A detailed description of these three models can be found in Petrus et al. (2024).

4.2. Optimized fitting strategy

The fits were performed using the code `ForMoSA`[2], which is based on a Bayesian algorithm known as nested sampling. This algorithm allows for a comprehensive exploration of the parameter space defined by the grids of synthetic spectra. This exploration is facilitated by calculating a likelihood function at each iteration, which is used to define N-dimensional isosurfaces (where N is the number of parameters being explored) that converge toward the maximum likelihood. In this analysis, we assume Gaussian and independent errors for the data, so maximizing the likelihood function is equivalent to minimizing a χ^2 function. This assumption may be incorrect for spectra that should include correlated noise, but to the best of our knowledge, no pipeline fully tracks the covariance to the science-ready spectra. In addition to the parameters considered by the grids, we extend the parameter space by exploring the radial velocity, which is performed by applying a Doppler shift to the synthetic spectra. The radius and distance are also constrained, serving as a dilution factor, $C_K = (R/d)^2$, between the synthetic flux generated at radius R and the data flux observed at distance d. A normal law is used as prior on the distance, with the mean value and standard deviation provided in Table 1. The other parameters are initialized with uniform priors summarized in Table 5. We used the nested sampling Python package `pyMultinest` (Buchner et al. 2014) and injected 200 living points during the inversion.

To evaluate the performance of models across the spectral types covered by X-SHYNE, we adapted the methodology of Petrus et al. (2024) to VLT/X-Shooter data, analyzing three distinct spectral windows independently. These windows correspond to the J (0.97–1.35 µm), H (1.41–1.85 µm), and K (1.95–2.48 µm) infrared bands. Additionally, we performed a combined fit across all three bands simultaneously, denoted as J+H+K. Due to limitations in the ability of the models to reproduce wavelengths shorter than 1 µm (Petrus et al. 2023), this range was excluded from our analysis. Unlike the approach in Petrus et al. (2024), in which the dispersion of the model predictions along the entire SED was exploited, we employed an alternative strategy. This assumes that the observed data error bars are insufficient to fully account for the discrepancies between the data and models. Our fitting routine consists of iterative loops that include the error inflation for the data, the spectral inversion, the computation of the reduced χ^2_{red} between the data and the best-fitting model, and the recalibration of the error inflation factor to scale χ^2_{red} to 1. If, after a spectral inversion, χ^2_{red} lies within [0.5, 1.5], the loop terminates, and the parameters are extracted from this final fit. Otherwise, a new iteration begins with the rescaled error bars. The spectral inversion employs a Bayesian algorithm, and the inflated data errors, which reflect the models' inability to fully reproduce the observations, are propagated into the parameter uncertainties. This concept aligns with the methodology implemented in the `Starfish` code (Czekala et al. 2015; Gully-Santiago et al. 2017), optimized to analyze stellar spectra, which calculates a covariance matrix for model grids using Gaussian process kernels and incorporates it into the likelihood calculation (Zhang et al. 2021c, Zhang et al. 2021d). While `Starfish` applies this as wavelength-dependent error inflation for each spectral channel, we simplified the approach by using a constant inflation factor across the wavelength range.

[2] https://formosa.readthedocs.io/

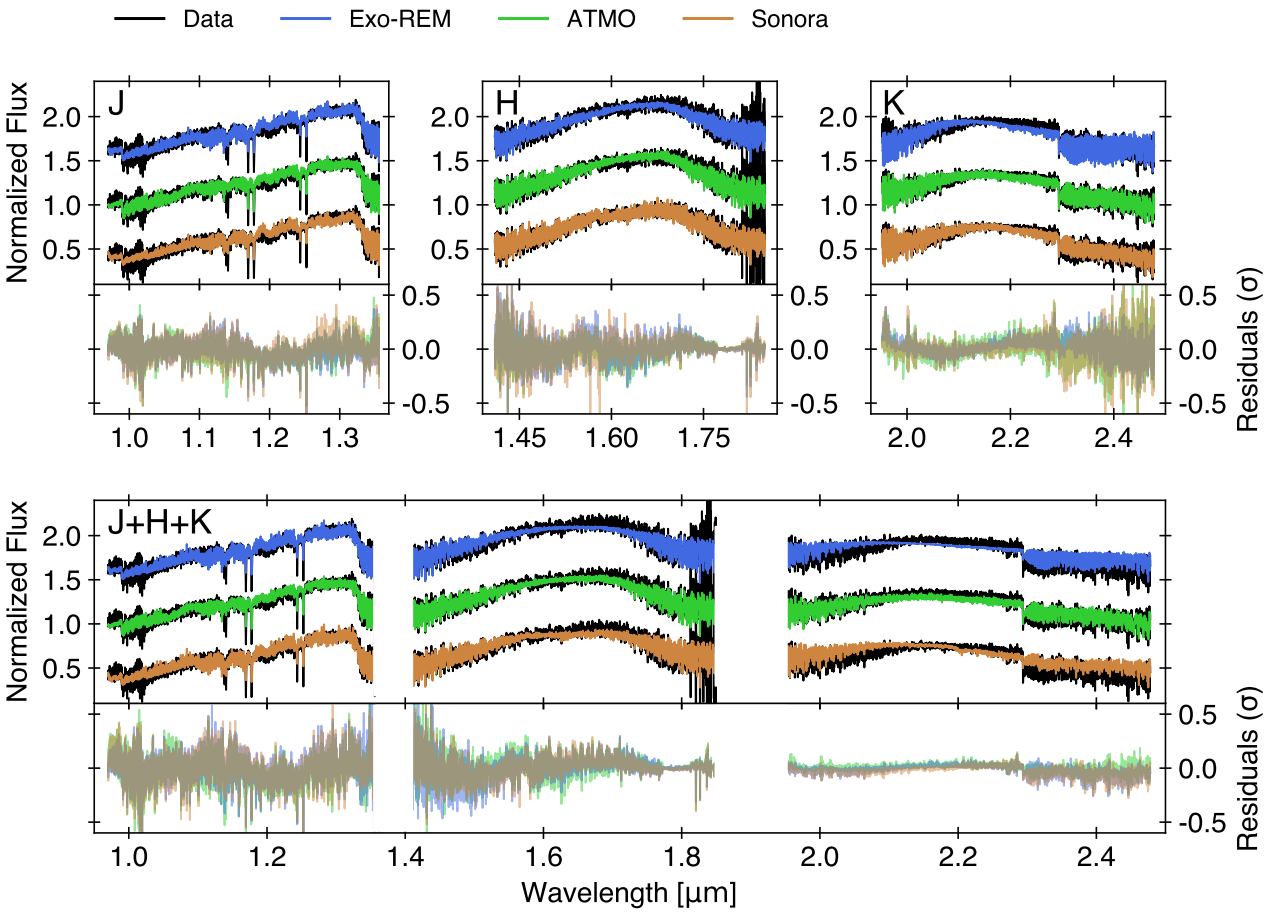

Fig. 5. Comparison between the X-Shooter spectra and the best fit obtained with each model when considering the J band (top-left panel), H band (top-center panel), and K band (top-right panel), as well as the combination of all bands (bottom panel). The example shown here is 2MASS 0046.

Incorporating the calculation of model covariance matrices into the `ForMoSA` framework will be addressed in a future update.

Despite optimizing our fitting strategy to ensure consistency between the synthetic spectra and the data, the posterior distribution of each parameter remains tightly constrained, resulting in unrealistically small uncertainties of <1 K for T_{eff} and <0.01 for log(g) and chemical abundances. Such small errors make the fit overly sensitive to minor irregularities in the model grid, potentially causing the posteriors to align with grid nodes and introducing biases.

To address this, we arbitrarily applied an inflation factor of 10, leading to revised uncertainties >10 K for T_{eff} and >0.05 for log(g) and chemical abundances. Since our analysis relies on precomputed grids of synthetic spectra, the fit results are primarily dictated by self-consistent model quality. Thus, inflating the observational errors does not affect the mean values of the posteriors but rather broadens their standard deviations. Furthermore, even with this inflation factor, our derived parameter uncertainties remain lower than those estimated in Petrus et al. (2024), where the parameter dispersion along the SED was considered. Consequently, the uncertainties on the parameters should be interpreted with caution, as they are likely still dominated by model systematics, which cannot be properly quantified. We also note that this inflation factor also encompasses the potential correlation between the errors of our spectra.

In summary, our fitting approach ensures convergence to the maximum likelihood, but as systematic errors remain difficult to quantify, the absolute uncertainties reported here do not fully capture these systematics. However, given the homogeneous nature of our analysis, the relative uncertainties across targets remain comparable.

4.3. Results

We applied `ForMoSA` to the 43 targets of X-SHYNE using the three different models described in Section 4.1 and considering the four wavelength ranges defined in Section 4.2. An example of a fit is shown in Figure 5, where the spectrum of 2MASS 0046 (L0) is overlaid with the synthetic spectra from each model that maximized the likelihood during the inversion. We observe that the quality of the model reproduction improves when each spectral band is considered separately. This confirms the findings of Petrus et al. (2024), who concluded that while models can accurately reproduce observational data locally, they fail to do so on a global wavelength range. We also note that, despite an improvement in the quality of the fit when shorter wavelength ranges are considered, certain spectral features, such as the depth of the potassium line, are not well reproduced. This issue was previously reported by Petrus et al. (2023), who performed dedicated fits to the potassium lines to partially correct the problem. We plan to conduct a similar synthetic analysis, focusing on medium-resolution spectral features, in future work.

5. Photometric anomaly

Since the late 1990s, photometric and spectroscopic observations have pointed to the presence of iron and silicate clouds

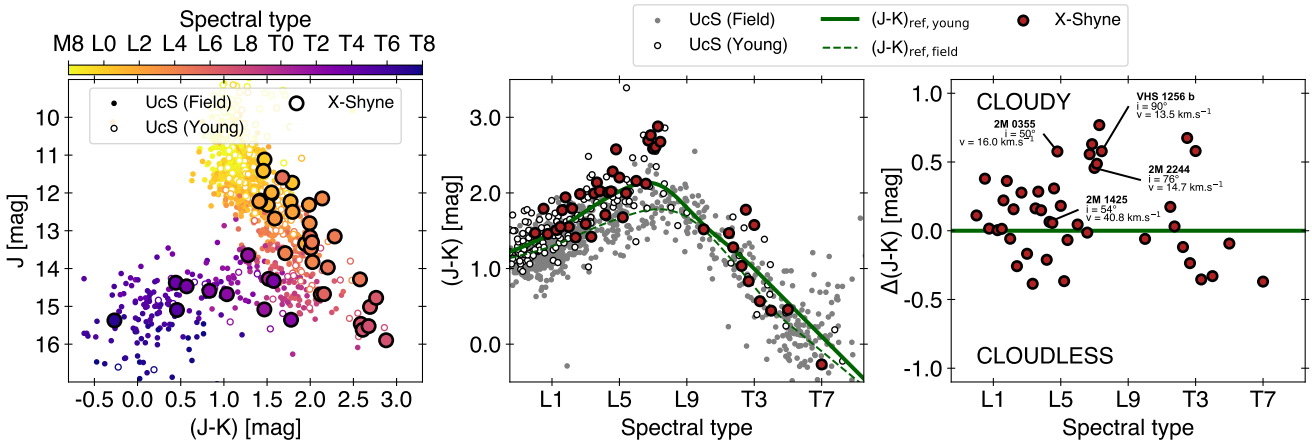

Fig. 6. Process used to calculate the photometric anomaly Δ(J-K). Left: Color-magnitude diagram of the L-T transition. We recalculated the J and K magnitudes for all targets from our X-Shooter spectra and compared them with objects from the UltraCoolSheet library. Center: We calculated (J–K) for each object and plotted it as a function of spectral type. The mean values for field and young objects from the UltraCoolSheet library are shown with dashed and solid green lines, respectively. Right: Δ(J-K) calculated as the offset from the mean (J-K) of young objects with the same spectral type. The four X-SHYNE objects for which rotational velocity and viewing angle measurements are available are highlighted. To improve the clarity of the plot, objects sharing the same spectral type have been evenly distributed within a range corresponding to their spectral type ±1.

in the photospheres of L-type brown dwarfs. These clouds help explain why these objects appear redder in color-magnitude diagrams (Tsuji et al. 1996; Ackerman & Marley 2001; Allard et al. 2001). These results indicates that clouds predominantly form in early L-type brown dwarfs before settling below the photosphere at the L-T transition as the temperature decreases. A few years later, large photometric time-monitoring surveys detected periodic variations in the infrared light curves of brown dwarfs. These variations were interpreted as inhomogeneities in cloud coverage that evolve with the object's rotation (Radigan et al. 2012; Apai et al. 2013; Zhou et al. 2016). Such analyses allow for the estimation of the rotational period (P). In combination with the projected rotational velocity (v sin(i)) derived from the broadening of atomic absorption lines detected via high-resolution spectroscopy, and the radius that can be inferred from models of evolution, it can be used to infer the viewing angle (i) of the observed targets. More recently, clouds have been directly detected through the exploration of mid-infrared wavelengths using the Spitzer Space Telescope and now the JWST. These observations revealed a broad silicate absorption feature around 10 μm (Suárez & Metchev 2022; Miles et al. 2023). By combining these silicate detections with photometric anomalies and viewing angles, (Suárez et al. 2023) highlighted a degeneracy among these parameters. This can be explained by the latitudinal dependence of dust cloud density, which is enhanced at the equator due to the object's rotation. This observational result confirms the predictions made by global circulation models, which indicate that cloud settling at the equator is enhanced with increasing rotational velocity (Tan & Showman 2021).

Consequently, brown dwarfs with similar fundamental properties (e.g., age, mass, T_{eff}) but viewed at different inclinations or with different rotational velocities could exhibit varying atmospheric properties when their spectra are compared with 1D atmospheric models. To account for this effect in our results, we quantified the amount of cloud coverage observed in our data. However, only 4 out of our 43 targets have a known viewing angle and silicate detection at 10 μm. Therefore, we calculated the Δ(J-K) color anomaly for all objects and used it as a proxy of the cloud density.

Given that brown dwarfs with these T_{eff} are expected to be variable, we aimed to calculate the color anomaly at the epoch of our observations. To do this, we extracted the J- and K-magnitudes from our X-Shooter data using the J- and K_s-2MASS filters and the flux-calibrated Vega spectrum to derive $(J-K)_{X-SHYNE}$. These photometric magnitudes were then compared to those in the UltracoolSheet library[3] (Best et al. 2021). For this comparison, we distinguished between objects showing signs of youth and field objects, as illustrated in the left panel of Figure 6. To establish reference (J − K) values for given spectral types of young and field objects, we applied a moving box method with a width of three spectral subtypes. This box was shifted across the spectral type range covered by the UltracoolSheet library, and the mean (J–K) was calculated for objects of each spectral type within the box. A Gaussian filter was then applied to smooth this curve and mitigate noise caused by a lack of objects at certain spectral types. For spectral types later than T3, the scarcity of young objects prevented us from calculating a mean (J–K). In these cases, we extrapolated the reference values by assuming a linear trend. Both the young and field $(J-K)_{ref}$ values are shown in the center panel of Figure 6, alongside the (J–K) values derived for X-SHYNE objects. Once again, we confirm the young age of X-SHYNE objects, which aligns well with the reference values of young objects from the UltracoolSheet library. We defined the color anomaly, Δ(J-K), as the difference $(J-K)_{X-SHYNE} - (J-K)_{ref,\ young}$ and calculated it for each X-SHYNE object.

These results are displayed in the right panel of Figure 6. A significant diversity in Δ(J-K) values is observed. One possible interpretation of this diversity lies in the variation in viewing angles and rotational velocities, two parameters that are presumed to be randomly distributed for directly imaged objects and remain independent of the observational epoch for isolated brown dwarfs and widely separated planetary-mass companions.

We have highlighted brown dwarfs for which estimates of the viewing angle and projected rotational velocity are available. Notably, 2MASS 0355 and 2MASS 1425 share similar spectral types (L3-L4) and viewing angles (50^{+2}_{-2}° Suárez et al. 2023 and 54^{+36}_{-15}° Vos et al. 2020, respectively) but exhibit different Δ(J-K) values. This discrepancy is consistent with their differing rotational velocities. For 2MASS 1425, its high

[3] https://zenodo.org/records/13993077

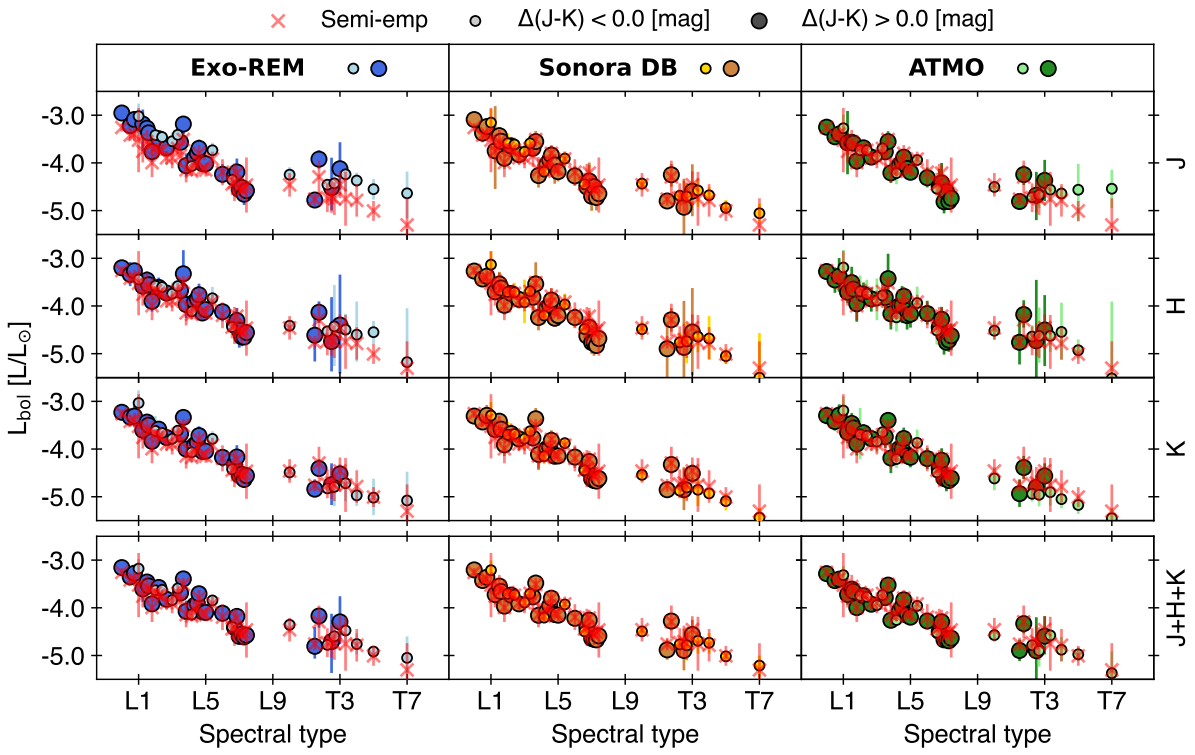

Fig. 7. L_{bol} estimated from each model grid and for each spectral range using the Stefan–Boltzmann law, based on the estimated T_{eff} (see Figure 8) and radius (see Figure 9). Objects with a negative color anomaly are represented by small light dots, while those with a positive color anomaly are shown as large deep dots. The L_{bol} values derived from the reconstructed SED (see Section 3.3) are indicated by red crosses.

rotational velocity (40.8 km s^{-1}) likely facilitates more efficient equatorial migration of clouds, in contrast to the slower-rotating 2MASS 0355. Similarly, VHS 1256 b and 2MASS 2244 have comparable spectral types (L7) and rotational velocities (13.5 and 14.7 km.s^{-1}, respectively), but VHS 1256 b shows a higher Δ(J-K) probably due to its equator-on viewing angle (Zhou et al. 2020), whereas 2MASS 2244 is observed at a lower inclination ($76^{+14\circ}_{-20}$ Vos et al. 2018). These trends seem to confirm a link between cloud density, viewing angle, and rotational velocity. However, the radius considered to estimate the inclination is model-dependent. Therefore, these results need to be confirmed by estimating these parameters for the remaining objects in the X-SHYNE sample following a homogeneous analysis. Moreover, the photometric anomaly could be influenced by the high variability of the objects, suggesting a variable cloud density along the longitudinal axis as well. For the remainder of this paper, we simplify the analysis by defining two regimes to qualitatively describe cloud density: Δ(J-K) > 0, corresponding to a cloudy viewing surface, and Δ(J-K) < 0, corresponding to a cloudless viewing surface.

6. Discussion

In Sections 3 and 4, we estimated the properties of the brown dwarfs in the X-SHYNE spectral library using the predictions of evolutionary and atmospheric models, respectively. In the case of evolutionary models, clouds are not considered, as the properties are derived from the cooling of brown dwarfs over time, driven by the lack of atomic fusion in their cores. It is now well established that clouds have a significant impact on the spectra of brown dwarfs and represent one of the major challenges for atmospheric models to address. In Section 5, we utilized the photometric anomaly, Δ(J-K), as a proxy for the impact of clouds along the line of sight. In this section, we discuss our estimates of the properties of X-SHYNE brown dwarfs derived from both approaches and examine the influence of clouds on these properties.

6.1. Bolometric luminosity, temperature and radius

Figures 7, 8, and 9 present the estimated values of L_{bol}, T_{eff}, and radius, respectively, for each object in X-SHYNE. The T_{eff} is derived from model grids, while the radius is inferred from the dilution factor C_K. The luminosity is calculated using the Stefan-Boltzmann law based on the T_{eff} and radius estimates, meaning it is not a free parameter in the Bayesian inversion. In each figure, the parameter values predicted by the evolutionary model (see Section 3) are represented by red crosses for direct comparison. For each model, the `ForMoSA` results distinguish between objects with a positive color anomaly (red excess) and those with a negative color anomaly (blue excess).

Figure 7 shows that, across all models and spectral bands, the luminosity derived from the synthetic analysis is consistent with the results described in Section 3.3. This confirms that self-consistent models can reliably estimate a target's bolometric luminosity, even when only a limited portion of the SED is available, as demonstrated in previous studies (e.g., Carter et al. 2023).

In contrast, Figure 8 highlights the limitations of the `Exo-REM` and `Sonora Diamondback` models in constraining T_{eff} for brown dwarfs earlier than L6, particularly when using the J or H bands, despite their grids extending to higher T_{eff} values. In Charnay et al. (2018), which presents the `Exo-REM` model, it is stated that the absence of certain condensates, such as Al_2O_3, or other absorbing species (e.g., ions) that significantly affect the atmosphere at higher T_{eff} (>1500 K), could lead to overly

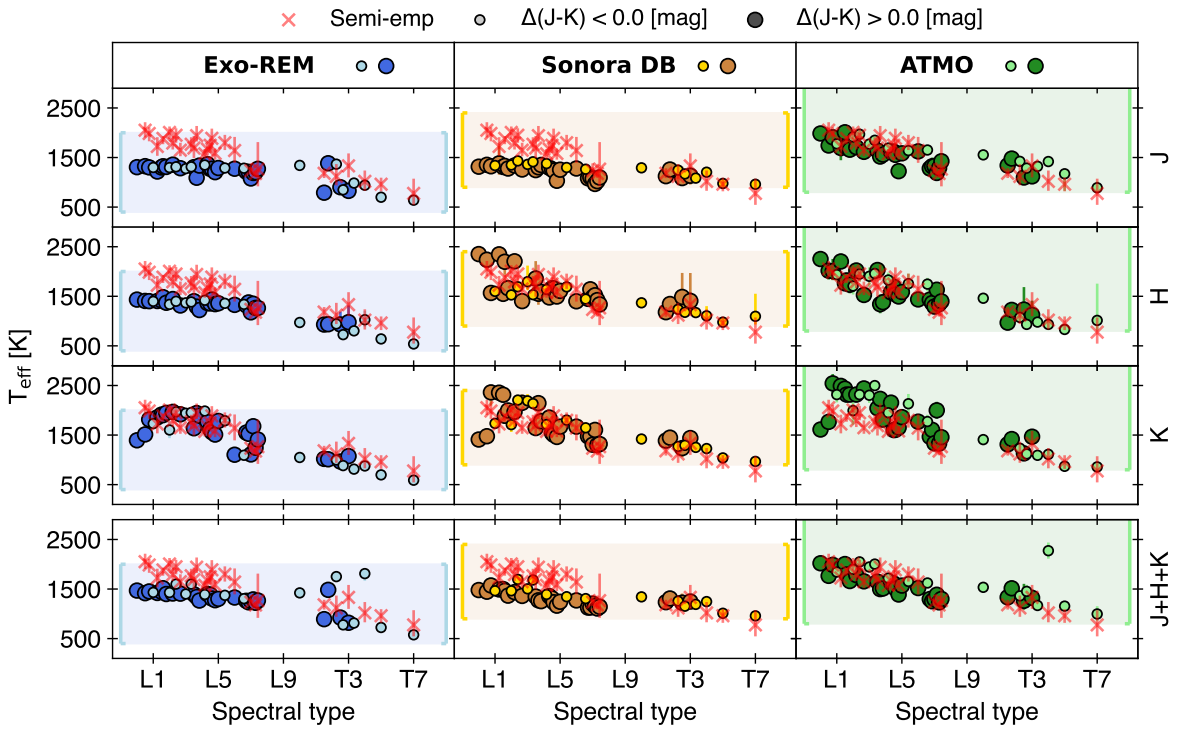

Fig. 8. Same as in Figure 7, but for the T_{eff}. The boundaries of each model grid are represented by the filled colored regions.

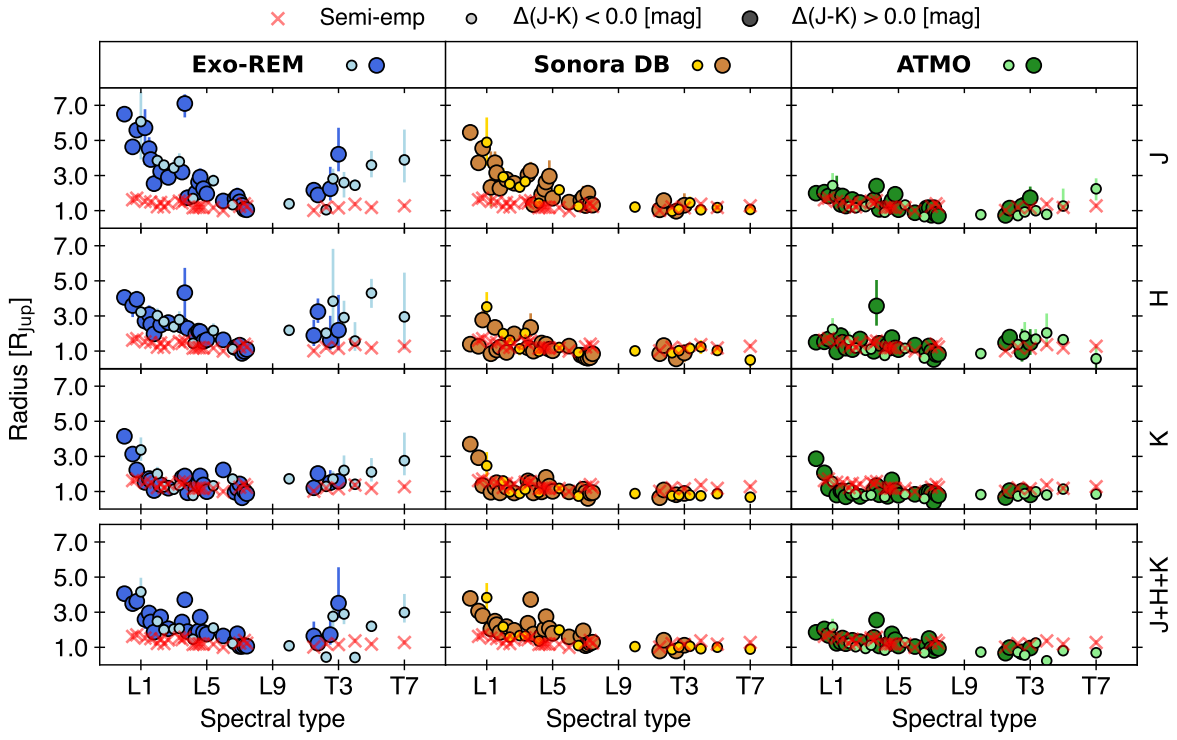

Fig. 9. Same as in Figure 7, but for the radius.

blue synthetic spectra. During spectral inversion, these biased synthetic spectra in the grid prevent likelihood maximization, even if their corresponding T_{eff} matches the evolutionary model predictions. Consequently, lower T_{eff} values around ~1500 K are favored, explaining the results in Figure 8. This result is in line with the study of Sanghi et al. (2023a) who also found a significant discrepancy between BT-SETTL atmospheric model and evolutionary models at the M-L transition due to a lack of absorbing species.

For `Sonora Diamondback`, a similar explanation applies, although the missing condensates may differ. Since Al_2O_3 clouds are included in this model, the T_{eff} values derived from H-band fits are more consistent with semiempirical estimates. However, when using the K band, both `Exo-REM` and

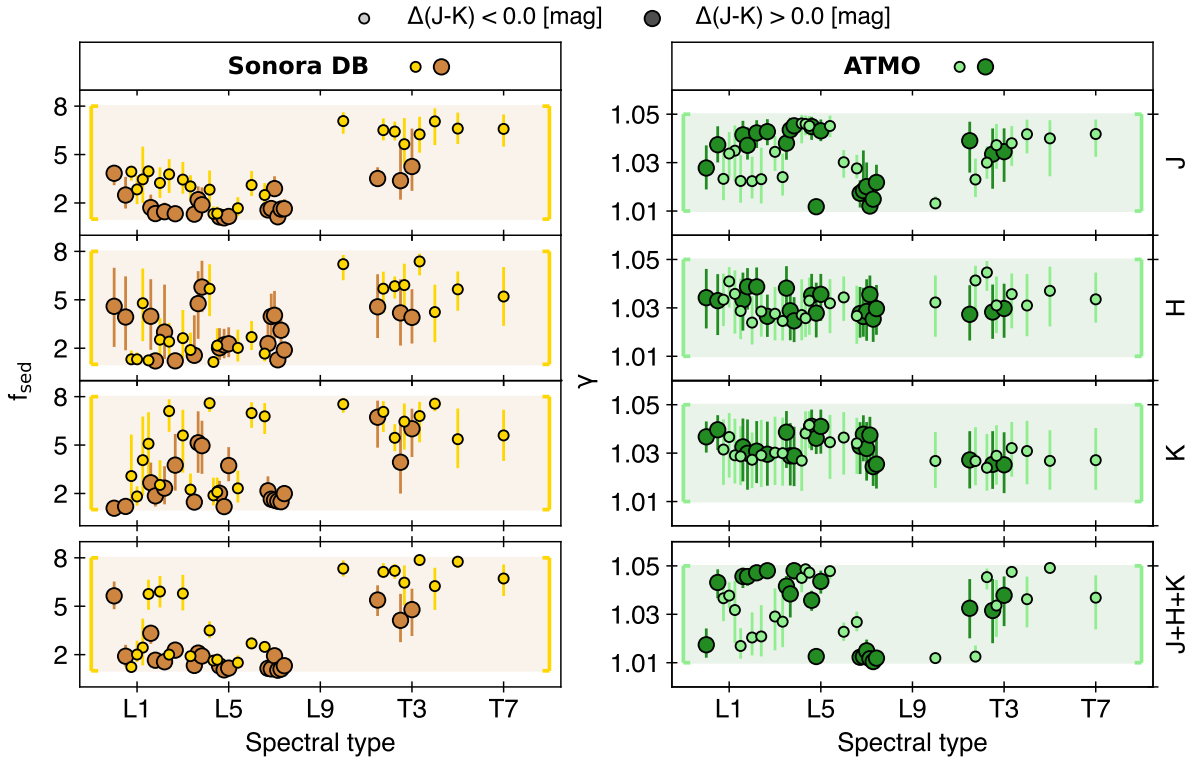

Fig. 10. Same as in Figure 7, but for the f_{sed} (left) and the γ (right). We notice that because these parameters are not considered in the evolutionary models, the red crosses are not present.

`Sonora Diamondback` yield T_{eff} estimates that align with evolutionary model predictions, indicating a reduced impact of missing species at these wavelengths.

For `ATMO`, the derived T_{eff} values agree with semiempirical results across all fit configurations except in the K band, where they appear overestimated. Unlike cloud-based models, `ATMO` replicates cloud effects through atmospheric instabilities (Tremblin et al. 2015, Tremblin et al. 2016). This alternative approach eliminates the issue of missing condensates, leading the spectral inversion to converge toward higher T_{eff} values.

The biases in T_{eff} observed for each model directly affect the estimated radius, which adjusts during inversion to maintain consistency with the bolometric luminosity of each object. Specifically, when T_{eff} is underestimated, the radius is overestimated, as shown in Figure 9.

Across all models, a trend emerges whereby objects with lower Δ(J-K) values appear hotter than those with higher Δ(J-K) values, particularly in the J band. If the color anomaly correlates with cloud density, this T_{eff} gradient could be explained by cloud absorption, which cools the upper atmospheric layers. In cases of negative color anomalies, low cloud densities enable deeper atmospheric layers, expected to be warmer, to become observable. However, this trend is not seen in T dwarfs, which is unsurprising since these cooler objects are expected to be cloud-free.

6.2. Cloud sedimentation and adiabatic index

To investigate the density of clouds observed in our sample, `Sonora Diamondback` allows us to explore different sedimentation efficiencies through its parameter f_{sed}, while `ATMO` provides a range of adiabatic index (γ) values that regulate the strength of atmospheric instabilities. In Figure 10, we plotted the estimated f_{sed}, and γ values for each object in X-SHYNE considering the different spectral bands.

As expected, before the L–T transition, we observe low f_{sed} values (< 2), indicating a cloudy atmosphere, whereas after the L-T transition, higher f_{sed} values (> 4) dominate, corresponding to lower cloud densities. Notably, bluer objects tend to have higher f_{sed} values compared to redder ones, supporting a correlation between this parameter and the color anomaly. Indeed, a lower value of f_{sed} means a cloudier atmosphere, and therefore a redder spectrum.

The trend for γ is less distinct. When considering the J-band and the full wavelength range, we find high γ values (> 1.03) before the L-T transition, indicating strong atmospheric instabilities, while post-transition values are more moderate ($\sim$1.03). However, this pattern is less pronounced in the H and K bands. Similar to f_{sed}, we generally observe lower γ values for bluer objects. This is expected since atmospheric instabilities directly contribute to the reddening of the spectra.

6.3. Surface gravity

All the models used here allow us to estimate log(g). In Figure 11, we observe that none of these models provide results fully consistent with the predictions of the evolutionary models. Moreover, these results are model-dependent, limiting our ability to determine a robust value for surface gravity. This issue has already been noted in previous multi-model analyses of single objects, such as Palma-Bifani et al. (2023) and Petrus et al. (2024). With X-SHYNE, we are able to capture and visualize these discrepancies across a wide range of spectral types.

The `Exo-REM` and `Sonora` models yield similar results, particularly when the J-band is used for the fit. A clear dependence on Δ(J–K) is observed, with redder objects displaying lower

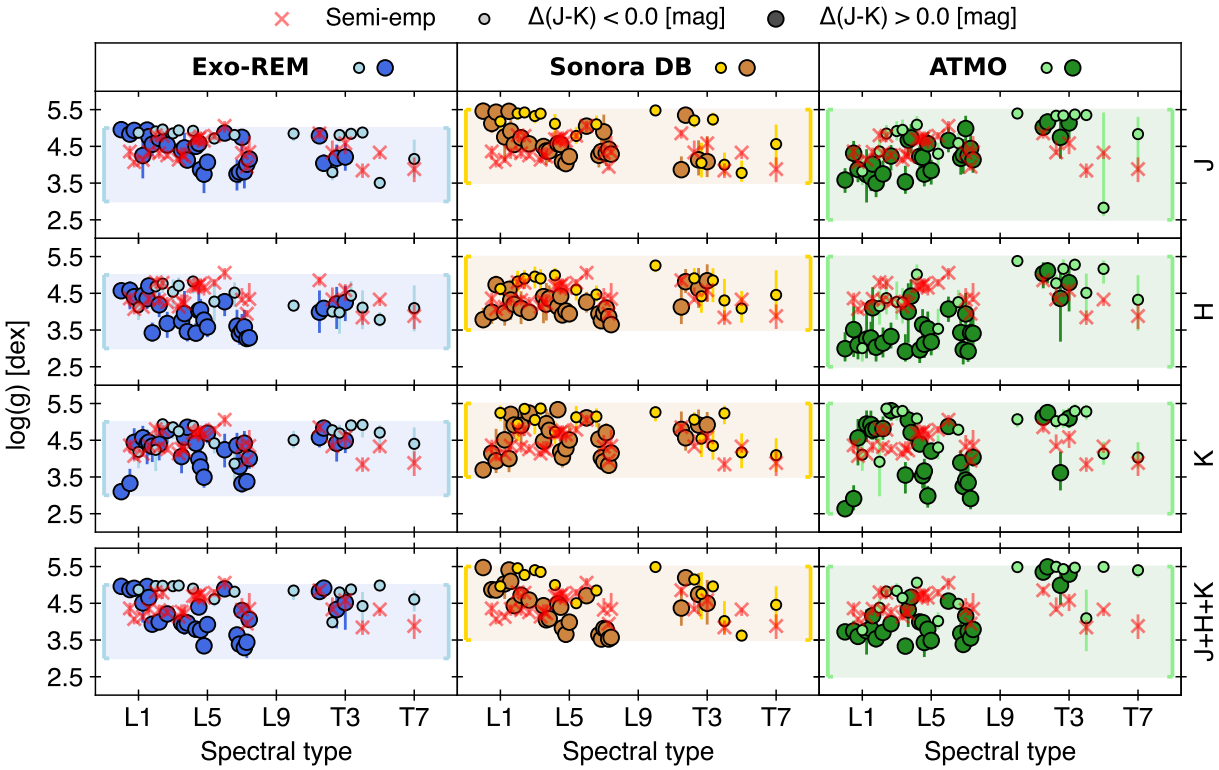

Fig. 11. Same as in Figure 7, but for the log(g).

log(g) than bluer ones. Low-gravity photospheres have lower pressure than high-gravity ones, resulting in reduced collision-induced absorptions (CIA) by H_2. Since CIA absorbs light over a broad range from the red end of the H band to most of the K band, low-log(g) models naturally appear redder in J-K. However, a similarly red J–K can also be produced by dust reddening, parameterized through f_{sed}, making log(g) and f_{sed} naturally degenerate when explaining Δ(J–K). A similar degeneracy should be detected with [M/H], as higher [M/H] increases absorption, leading to a higher altitude for the photosphere. This results in a lower-pressure environment, similar to the effect of low-log(g), thereby reducing CIA absorption. Consequently, [M/H], dust, and log(g) are all degenerate when interpreting Δ(J–K). We can see this effect of Δ(J–K) on the [M/H] in Figure C.1.

We highlight that since log(g) does not strongly affect spectra beyond this CIA-related impact, it is possible that models primarily determine log(g) based on the residual Δ(J–K) after fitting for dust and [M/H]. This could lead to a wide dispersion in estimated log(g) values, not because log(g) varies significantly across the sample, but because it is the most flexible parameter to accommodate the Δ(J–K). We also notice that the ATMO model does not exhibit a clear correlation between log(g) and Δ(J–K), as the reddening effect is primarily driven by the adiabatic index γ, which governs atmospheric instabilities.

From the perspective of evolutionary models, surface gravity is calculated based on mass and radius. The latter decreases with age, leading to an increase in log(g). However, this approach does not account for the atmospheric complexities reflected in the diversity of Δ(J–K). Because these two different log(g) do not describe the same physical processes, comparing them may lead to significant discrepancies, which could explain the differences observed in Figure 11.

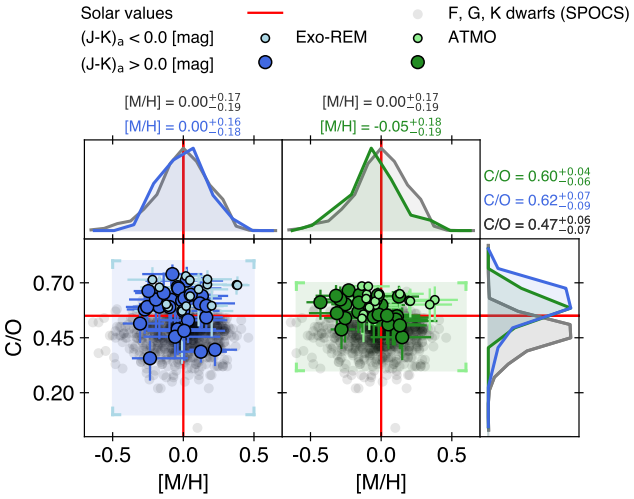

Fig. 12. C/O and [M/H] estimated from the ATMO and Exo-REM grids when considering the K band. We overlaid our results for the X-SHYNE library with the abundance estimates from the cool stars in the SPOCS catalog. To facilitate the comparison between both samples, we plotted the distributions of [M/H] and C/O in the right and top panels, respectively. We also provide the mean value and the 1-σ standard deviation of each distribution.

6.4. Metallicity and carbon-to-oxygen ratio

The relative chemical abundances, C/O and [M/H], are explored in both the Exo-REM and ATMO grids. We compared their estimates when the K-band is considered in Figure 12. This band is expected to be the most sensitive to C/O given the absorptions of CO and H2O in this band. Previous studies have shown that CO

overtones at ~2.3 μm are key features for constraining the C/O ratio (Konopacky et al. 2013, Nowak et al. 2020, Petrus et al. 2021, Hoch et al. 2022, Petrus et al. 2023). The results for each fitting configuration can be found in Appendix C.1.

From our synthetic analysis, we observe a significant dispersion in the estimated C/O and [M/H] values within the X-SHYNE library. Additionally, the distribution is centered around solar values, suggesting that, overall, the objects of X-SHYNE exhibit solar-like relative abundances.

We also compared our results with the chemical abundances of cool stars from the SPOCS catalog (Valenti & Fischer 2005), which contains properties of 1040 nearby F, G, and K stars observed through the Keck, Lick, and AAT planet search programs. We used the [M/H] values from Valenti & Fischer (2005) and the C/O estimates from Brewer & Fischer (2016). Our findings indicate that both `Exo-REM` and `ATMO` yield metallicities similar to the ones of the SPOCS population but suggest slightly higher C/O ratios. Several factors could explain this discrepancy. One possibility is that the X-SHYNE objects formed through different processes than those in the SPOCS catalog, possibly involving enrichment from disk material. However, since our objects are isolated, this scenario is unlikely. Alternatively, systematic errors in the models could introduce biases. Both models assume solar abundances as initial conditions due to the unknown birth environments of the observed objects. However, Brewer & Fischer (2016) show that the C/O measured for the Sun is higher than the C/O measured for the stars from the SPOCS sample. Moreover, spectral data only provide information about the photosphere, meaning the measured abundances may not fully reflect the bulk composition of the objects (Helling et al. 2014). Indeed, oxygen can be trapped into clouds and then removed from the photosphere with cloud sedimentation. In the context of past and future characterization of imaged planets or young brown dwarfs, the X-SHYNE library offers for the first time a real demographic anchor point for confirming any significant compositional departure that could be linked to heavy element enrichment mechanisms connected to planetary formation processes.

7. Summary and conclusion

In this paper, we exploited the medium-resolution ($R_\lambda \sim 8100$) near-infrared (0.3–2.5 μm) spectra of 43 young, low-mass brown dwarfs through a semiempirical and synthetic analysis. With the semiempirical approach we have calculated the bolometric luminosity of each target by integrating their SED by adapting the method described in Filippazzo et al. (2015). For objects identified as members of young moving groups, we injected the L_{bol} and the age of these associations into a model of the evolution to estimate the T_{eff}, mass, radius, and log(g) of our objects. The synthetic analysis was performed with the code `ForMoSA` considering the three grids of precomputed synthetic spectra, `Exo-REM`, `ATMO`, and `Sonora Diamondback`.

This methodology enabled us to perform a global comparative analysis, following three types of investigation:

– A comparison between evolutionary models and atmospheric models: The L_{bol} estimates from the two approaches are similar. We observe the limitations of the cloudy models, `Exo-REM` and `Sonora`, which fail to reach $T_{eff} > 1500$ K when the J or H bands are considered due to a lack of absorbers in the simulated atmosphere. In contrast, `ATMO` provides T_{eff} values consistent with evolutionary models. Consequently, when T_{eff} is underestimated, the radius is overestimated. Lastly, the log(g), which represents different physical processes in each type of model, appears to be inconsistent between the two approaches;
– A comparison between different atmospheric models: We observe a dispersion in the surface gravity estimates derived from the cloudy models `Exo-REM` and `Sonora`, particularly for objects with spectral types ranging from L4 to L7, where clouds are expected to dominate. This dispersion is not present in the cloudless model `ATMO`. We interpret this as direct evidence of a diversity in cloud densities, driven by variations in rotational velocity, which influence cloud migration toward the equator, and a range of viewing latitudes (inclinations). This interpretation is supported by the calculation of a color anomaly, which depends on cloud density and the sedimentation factor explored in `Sonora`, where cloudier atmospheres exhibit a lower sedimentation efficiency;
– A comparison between the objects of X-SHYNE: We confirm the decrease in L_{bol} with spectral type. Additionally, we observe a lower f_{sed} for L-type objects, indicating a cloudy atmosphere, and a higher f_{sed} for T-type objects, consistent with a cloudless atmosphere. The estimated relative chemical abundances, C/O and [M/H], exhibit significant dispersion within the X-SHYNE library, making it difficult to provide robust estimates for individual objects. However, the diversity of the sample allows us to discuss the overall chemical composition of X-SHYNE, which suggests solar values. The metallicity aligns well with measurements from a population of F, G, and K stars, while the C/O ratio derived from X-SHYNE appears to be higher. This offset could be attributed to a systematic bias related to the initial chemical abundances assumed in the self-consistent atmospheric models or to the difference between the measured C/O, representative of the photosphere, and the bulk C/O of the objects. Finally, the X-SHYNE library provides for the first time a true demographic anchor for the chemical composition of a population of young brown dwarfs, or so-called exoplanet analogs, given their mass overlap with directly imaged planets. This study can confirm any significant compositional departure from a population that is likely formed via stellar mechanisms and that could be related to heavy element enrichment mechanisms associated with planetary formation processes.

These results highlight the strength of comparative analysis using homogeneous datasets of a diverse sample of objects to identify model limitations and derive robust conclusions, while minimizing overinterpretation. A complementary study should be conducted in the future to confirm the impact of inclination on atmospheric characterization by incorporating high-resolution data to estimate rotational velocity and mid-infrared spectroscopy to quantify silicate cloud density. Additionally, a combined atmospheric model that integrates both cloud formation and atmospheric instabilities should be considered to accurately reproduce the spectra of L dwarfs and derive physically consistent atmospheric parameters.

Data availability

The numerical values of the EWs estimated for the four potassium lines in Section 3.2, the photometric anomaly Δ(J–K) estimated in Section 5, and the properties of the objects of X-Shyne obtained with `ForMoSA` in Section 4 are available at the CDS via https://cdsarc.cds.unistra.fr/viz-bin/cat/J/A+A/701/A208. The spectra presented in the article are also available following the same CDS reference.

Acknowledgements. We would like to thank the staff of ESO VLT for their support at the telescope at Paranal and La Silla, and the preparation of the observation at Garching. This publication made use of the SIMBAD and VizieR database operated at the CDS, Strasbourg, France. This work has made use of data from the European Space Agency (ESA) mission Gaia (https://www.cosmos.esa.int/gaia), processed by the Gaia Data Processing and Analysis Consortium (DPAC, https://www.cosmos.esa.int/web/gaia/dpac/consor576utium). Funding for the DPAC has been provided by national institutions, in particular the institutions participating in the Gaia Multilateral Agreement. We acknowledge support in France from the French National Research Agency (ANR) through project grants ANR-14-CE33-0018 and ANR-20-CE31-0012. This publication makes use of VOSA, developed under the Spanish Virtual Observatory (https://svo.cab.inta-csic.es) project funded by MCIN/AEI/10.13039/501100011033/ through grant PID2020-112949GB-I00. VOSA has been partially updated by using funding from the European Union's Horizon 2020 Research and Innovation Programme, under Grant Agreement Nr. 776403 (EXOPLANETS-A). This work has benefitted from The UltracoolSheet at http://bit.ly/UltracoolSheet, maintained by Will Best, Trent Dupuy, Michael Liu, Aniket Sanghi, Rob Siverd, and Zhoujian Zhang, and developed from compilations by Dupuy & Liu (2012), Dupuy & Kraus (2013), Deacon et al. (2014), Liu et al. (2016), Best et al. (2018), Best et al. (2021), Sanghi et al. (2023b), and Schneider et al. (2023). S.P. is supported by the ANID FONDECYT Postdoctoral program No. 3240145. The authors acknowledge support from ANID – Millennium Science Initiative Program – Center Code NCN2024_001. J.-S.J. gratefully acknowledges support from FONDECYT grant 1240738 and from the ANID BASAL project FB210003. G.-D.M. acknowledges the support of the DFG priority program SPP 1992 "Exploring the Diversity of Extrasolar Planets" (MA 9185/1), from the European Research Council (ERC) under the Horizon 2020 Framework Program via the ERC Advanced Grant "ORIGINS" (PI: Henning), No. 832428, and via the research and innovation programme "PROTOPLANETS", grant agreement No. 101002188 (PI: Benisty). Parts of this work have been carried out within the framework of the NCCR PlanetS supported by the Swiss National Science Foundation. Z.Z. acknowledges the support of the NASA Hubble Fellowship grant HST-HF2-51522.001-A. A.B. acknowledges the Deutsche Forschungsgemeinschaft's (DFG, German Research Foundation) support under Germany's Excellence Strategy – EXC 2094 – 390783311. M.C.L. acknowledges the Gordon and Betty Moore Foundation through grant GBMF8550 that funded a part of this work.

References

Ackerman, A. S., & Marley, M. S. 2001, ApJ, 556, 872
Allard, F., Hauschildt, P. H., Alexander, D. R., Tamanai, A., & Schweitzer, A. 2001, ApJ, 556, 357
Allers, K. N., & Liu, M. C. 2013, ApJ, 772, 79
Aller, K. M., Liu, M. C., Magnier, E. A., et al. 2016, ApJ, 821, 120
Almendros-Abad, V., Mužić, K., Moitinho, A., Krone-Martins, A., & Kubiak, K. 2022, A&A, 657, A129
Apai, D., Radigan, J., Buenzli, E., et al. 2013, ApJ, 768, 121
Artigau, É., Doyon, R., Lafrenière, D., et al. 2006, ApJ, 651, L57
Artigau, É., Gagné, J., Faherty, J., et al. 2015, ApJ, 806, 254
Baraffe, I., Chabrier, G., Barman, T. S., Allard, F., & Hauschildt, P. H. 2003, A&A, 402, 701
Barnes, S. A. 2009, in IAU Symposium, 258, The Ages of Stars, eds. E. E. Mamajek, D. R. Soderblom, & R. F. G. Wyse, 345
Bayo, A., Barrado, D., Stauffer, J., et al. 2011, A&A, 536, A63
Bell, C. P. M., Mamajek, E. E., & Naylor, T. 2015, MNRAS, 454, 593
Best, W. M. J., Liu, M. C., Magnier, E. A., et al. 2015, ApJ, 814, 118
Best, W. M. J., Liu, M. C., Dupuy, T. J., & Magnier, E. A. 2017, ApJ, 843, L4
Best, W. M. J., Magnier, E. A., Liu, M. C., et al. 2018, ApJS, 234, 1
Best, W. M. J., Liu, M. C., Magnier, E. A., & Dupuy, T. J. 2020, AJ, 159, 257
Best, W. M. J., Liu, M. C., Magnier, E. A., & Dupuy, T. J. 2021, AJ, 161, 42
Beuzit, J. L., Vigan, A., Mouillet, D., et al. 2019, A&A, 631, A155
Böker, T., Arribas, S., Lützgendorf, N., et al. 2022, A&A, 661, A82
Bonnefoy, M., Chauvin, G., Lagrange, A. M., et al. 2014, A&A, 562, A127
Bowler, B. P., Zhou, Y., Morley, C. V., et al. 2020, ApJ, 893, L30
Brewer, J. M., & Fischer, D. A. 2016, ApJ, 831, 20
Buchner, J., Georgakakis, A., Nandra, K., et al. 2014, A&A, 564, A125
Burgasser, A. J., Kirkpatrick, J. D., Brown, M. E., et al. 2002a, ApJ, 564, 421
Burgasser, A. J., Marley, M. S., Ackerman, A. S., et al. 2002b, ApJ, 571, L151
Burgasser, A. J., Geballe, T. R., Leggett, S. K., Kirkpatrick, J. D., & Golimowski, D. A. 2006, ApJ, 637, 1067
Burgasser, A. J., Lopez, M. A., Mamajek, E. E., et al. 2016, ApJ, 820, 32
Carter, A. L., Hinkley, S., Kammerer, J., et al. 2023, ApJ, 951, L20
Charnay, B., Bézard, B., Baudino, J. L., et al. 2018, ApJ, 854, 172
Chauvin, G., Desidera, S., Lagrange, A. M., et al. 2017, A&A, 605, L9
Cruz, K. L., Reid, I. N., Liebert, J., Kirkpatrick, J. D., & Lowrance, P. J. 2003, AJ, 126, 2421
Cruz, K. L., Reid, I. N., Kirkpatrick, J. D., et al. 2007, AJ, 133, 439
Cruz, K. L., Núñez, A., Burgasser, A. J., et al. 2018, AJ, 155, 34
Cushing, M. C., Rayner, J. T., & Vacca, W. D. 2005, ApJ, 623, 1115
Cushing, M. C., Marley, M. S., Saumon, D., et al. 2008, ApJ, 678, 1372
Cushing, M. C., Looper, D., Burgasser, A. J., et al. 2009, ApJ, 696, 986
Cutri, R. M., & et al. 2012, VizieR Online Data Catalog: WISE All-Sky Data Release (Cutri+ 2012), VizieR On-line Data Catalog: II/311. Originally published in: 2012wise.rept....1C
Czekala, I., Andrews, S. M., Mandel, K. S., Hogg, D. W., & Green, G. M. 2015, ApJ, 812, 128
Dahn, C. C., Harris, H. C., Vrba, F. J., et al. 2002, AJ, 124, 1170
Davies, R., Absil, O., Agapito, G., et al. 2023, A&A, 674, A207
Day-Jones, A. C., Marocco, F., Pinfield, D. J., et al. 2013, MNRAS, 430, 1171
Deacon, N. R., Liu, M. C., Magnier, E. A., et al. 2014, ApJ, 792, 119
Desgrange, C., Chauvin, G., Christiaens, V., et al. 2022, A&A, 664, A139
Dieterich, S. B., Henry, T. J., Jao, W.-C., et al. 2014, AJ, 147, 94
Dupuy, T. J., & Kraus, A. L. 2013, Science, 341, 1492
Dupuy, T. J., & Liu, M. C. 2012, ApJS, 201, 19
Dupuy, T. J., Liu, M. C., Allers, K. N., et al. 2018, AJ, 156, 57
Dupuy, T. J., Liu, M. C., Magnier, E. A., et al. 2020, RNAAS, 4, 54
Dupuy, T. J., Liu, M. C., Evans, E. L., et al. 2023, MNRAS, 519, 1688
Eisenhauer, F., Abuter, R., Bickert, K., et al. 2003, SPIE Conf. Ser., 4841, 1548
Faherty, J. K., Burgasser, A. J., Cruz, K. L., et al. 2009, AJ, 137, 1
Faherty, J. K., Burgasser, A. J., Walter, F. M., et al. 2012, ApJ, 752, 56
Faherty, J. K., Riedel, A. R., Cruz, K. L., et al. 2016, ApJS, 225, 10
Filippazzo, J. C., Rice, E. L., Faherty, J., et al. 2015, ApJ, 810, 158
Freudling, W., Romaniello, M., Bramich, D. M., et al. 2013, A&A, 559, A96
Gagné, J. 2024, PASP, 136, 063001
Gagné, J., & Faherty, J. K. 2018, ApJ, 862, 138
Gagné, J., Faherty, J. K., Cruz, K., et al. 2014, ApJ, 785, L14
Gagné, J., Faherty, J. K., Cruz, K. L., et al. 2015a, ApJS, 219, 33
Gagné, J., Faherty, J. K., Cruz, K. L., et al. 2015b, ApJS, 219, 33
Gagné, J., Faherty, J. K., Mamajek, E. E., et al. 2017, ApJS, 228, 18
Gagné, J., Mamajek, E. E., Malo, L., et al. 2018, ApJ, 856, 23
Gaia Collaboration. 2020, VizieR Online Data Catalog: Gaia EDR3 (Gaia Collaboration, 2020), VizieR On-line Data Catalog: I/350. Originally published in: 2021A&A...649A...1G
Gauza, B., Béjar, V. J. S., Pérez-Garrido, A., et al. 2015, ApJ, 804, 96
Geballe, T. R., Knapp, G. R., Leggett, S. K., et al. 2002, ApJ, 564, 466
Golimowski, D. A., Leggett, S. K., Marley, M. S., et al. 2004, AJ, 127, 3516
GRAVITY Collaboration (Abuter, R., et al.) 2017, A&A, 602, A94
Gully-Santiago, M. A., Herczeg, G. J., Czekala, I., et al. 2017, ApJ, 836, 200
Helling, C., Woitke, P., Rimmer, P. B., et al. 2014, Life, 4, 142
Hoch, K. K. W., Konopacky, Q. M., Barman, T. S., et al. 2022, AJ, 164, 155
Hurt, S. A., Liu, M. C., Zhang, Z., et al. 2024, ApJ, 961, 121
Jovanovic, N., Guyon, O., Lozi, J., et al. 2016, SPIE Conf. Ser., 9909, 99090W
Kaeufl, H.-U., Ballester, P., Biereichel, P., et al. 2004, SPIE Conf. Ser., 5492, 1218
Kausch, W., Noll, S., Smette, A., et al. 2015, A&A, 576, A78
Kellogg, K., Metchev, S., Geißler, K., et al. 2015, AJ, 150, 182
Kendall, T. R., Delfosse, X., Martín, E. L., & Forveille, T. 2004, A&A, 416, L17
Kirkpatrick, J. D., Cushing, M. C., Gelino, C. R., et al. 2011, ApJS, 197, 19
Kirkpatrick, J. D., Reid, I. N., Liebert, J., et al. 1999, ApJ, 519, 802
Kirkpatrick, J. D., Reid, I. N., Liebert, J., et al. 2000, AJ, 120, 447
Kirkpatrick, J. D., Gelino, C. R., Faherty, J. K., et al. 2021, ApJS, 253, 7
Knapp, G. R., Leggett, S. K., Fan, X., et al. 2004, AJ, 127, 3553
Konopacky, Q. M., Barman, T. S., Macintosh, B. A., & Marois, C. 2013, Science, 339, 1398
Kotani, T., Kawahara, H., Ishizuka, M., et al. 2020, SPIE Conf. Ser., 11448, 1144878
Larkin, J., Barczys, M., Krabbe, A., et al. 2006, SPIE Conf. Ser., 6269, 62691A
Liu, M. C., Magnier, E. A., Deacon, N. R., et al. 2013, ApJ, 777, L20
Liu, M. C., Dupuy, T. J., & Allers, K. N. 2016, ApJ, 833, 96
Lodieu, N., Zapatero Osorio, M. R., Béjar, V. J. S., & Peña Ramírez, K. 2018, MNRAS, 473, 2020
Lopez, B., Lagarde, S., Petrov, R. G., et al. 2022, A&A, 659, A192
Lucas, P. W., Roche, P. F., Allard, F., & Hauschildt, P. H. 2001, MNRAS, 326, 695
Macintosh, B., Graham, J. R., Ingraham, P., et al. 2014, PNAS, 111, 12661
Macintosh, B., Graham, J. R., Barman, T., et al. 2015, Science, 350, 64
Mamajek, E. E. 2009, in IAU Symposium, 258, The Ages of Stars, eds. E. E. Mamajek, D. R. Soderblom, & R. F. G. Wyse, 375
Manjavacas, E., Lodieu, N., Béjar, V. J. S., et al. 2020, MNRAS, 491, 5925
Marley, M. S., Saumon, D., & Goldblatt, C. 2010, ApJ, 723, L117
Marocco, F., Day-Jones, A. C., Lucas, P. W., et al. 2014, MNRAS, 439, 372
Marocco, F., Jones, H. R. A., Day-Jones, A. C., et al. 2015, MNRAS, 449, 3651

Marocco, F., Eisenhardt, P. R. M., Fowler, J. W., et al. 2021, ApJS, 253, 8
Martin, E. C., Mace, G. N., McLean, I. S., et al. 2017, ApJ, 838, 73
Martín, E. L., Delfosse, X., Basri, G., et al. 1999, AJ, 118, 2466
Matthews, E. C., Mollière, P., Kühnle, H., et al. 2025, ApJ, 981, L31
Mawet, D., Ruane, G., Xuan, W., et al. 2017, ApJ, 838, 92
McCaughrean, M. J., & Pearson, S. G. 2023, arXiv e-prints [arXiv:2310.03552]
Mesa, D., Gratton, R., Kervella, P., et al. 2023, A&A, 672, A93
Michaud, G., & Charbonneau, P. 1991, Space Sci. Rev., 57, 1
Miles, B. E., Biller, B. A., Patapis, P., et al. 2023, ApJ, 946, L6
Modigliani, A., Goldoni, P., Royer, F., et al. 2010, SPIE Conf. Ser., 7737, 773728
Mollière, P., Molyarova, T., Bitsch, B., et al. 2022, ApJ, 934, 74
Moranta, L., Gagné, J., Couture, D., & Faherty, J. K. 2022, ApJ, 939, 94
Morley, C. V., Mukherjee, S., Marley, M. S., et al. 2024, arXiv e-prints, [arXiv:2402.00758]
Nordström, B., Mayor, M., Andersen, J., et al. 2004, A&A, 418, 989
Nowak, GRAVITY Collaboration, M., Lacour, S., et al. 2020, A&A, 633, A110
Öberg, K. I., Murray-Clay, R., & Bergin, E. A. 2011, ApJ, 743, L16
Ormel, C. W., Vazan, A., & Brouwers, M. G. 2021, A&A, 647, A175
Palma-Bifani, P., Chauvin, G., Bonnefoy, M., et al. 2023, A&A, 670, A90
Palma-Bifani, P., Chauvin, G., Borja, D., et al. 2024, A&A, 683, A214
Peters-Limbach, M. A., Groff, T., Kasdin, N. J., et al. 2012, SPIE Conf. Ser., 8446, 84467U
Petrus, S., Bonnefoy, M., Chauvin, G., et al. 2020, A&A, 633, A124
Petrus, S., Bonnefoy, M., Chauvin, G., et al. 2021, A&A, 648, A59
Petrus, S., Chauvin, G., Bonnefoy, M., et al. 2023, A&A, 670, L9
Petrus, S., Whiteford, N., Patapis, P., et al. 2024, ApJ, 966, L11
Piscarreta, L., Mužić, K., Almendros-Abad, V., & Scholz, A. 2024, A&A, 686, A37
Radigan, J., Jayawardhana, R., Lafrenière, D., et al. 2012, ApJ, 750, 105
Rebolo, R. 1991, in IAU Symposium, 145, Evolution of Stars: the Photospheric Abundance Connection, eds. G. Michaud, & A. V. Tutukov, 85
Reid, I. N., Lewitus, E., Allen, P. R., Cruz, K. L., & Burgasser, A. J. 2006, AJ, 132, 891
Reid, I. N., Cruz, K. L., Kirkpatrick, J. D., et al. 2008, AJ, 136, 1290
Samland, M., Mollière, P., Bonnefoy, M., et al. 2017, A&A, 603, A57
Sanghi, A., Liu, M. C., Best, W. M. J., et al. 2023a, ApJ, 959, 63
Sanghi, A., Liu, M. C., Best, W. M. J., et al. 2023b, ApJ, 959, 63
Schneider, A. C., Munn, J. A., Vrba, F. J., et al. 2023, AJ, 166, 103
Schneider, A. C., Windsor, J., Cushing, M. C., Kirkpatrick, J. D., & Shkolnik, E. L. 2017, AJ, 153, 196
Skumanich, A. 1972, ApJ, 171, 565
Smart, R. L., Tinney, C. G., Bucciarelli, B., et al. 2013, MNRAS, 433, 2054
Smette, A., Sana, H., Noll, S., et al. 2015, A&A, 576, A77
Snellen, I. A. G., Brandl, B. R., de Kok, R. J., et al. 2014, Nature, 509, 63
Soderblom, D. R., Duncan, D. K., & Johnson, D. R. H. 1991, ApJ, 375, 722
Stephens, D. C., Leggett, S. K., Cushing, M. C., et al. 2009, ApJ, 702, 154
Suárez, G., & Metchev, S. 2022, MNRAS, 513, 5701
Suárez, G., Vos, J. M., Metchev, S., Faherty, J. K., & Cruz, K. 2023, ApJ, 954, L6
Tan, X., & Showman, A. P. 2021, MNRAS, 502, 2198
Tinney, C. G., Faherty, J. K., Kirkpatrick, J. D., et al. 2014, ApJ, 796, 39
Tinney, C. G., Kirkpatrick, J. D., Faherty, J. K., et al. 2018, ApJS, 236, 28
Torres, C. A. O., Quast, G. R., Melo, C. H. F., & Sterzik, M. F. 2008, in Handbook of Star Forming Regions, Volume II, 5, ed. B. Reipurth, 757
Tremblin, P., Amundsen, D. S., Mourier, P., et al. 2015, ApJ, 804, L17
Tremblin, P., Amundsen, D. S., Chabrier, G., et al. 2016, ApJ, 817, L19
Tsuji, T., Ohnaka, K., Aoki, W., & Nakajima, T. 1996, A&A, 308, L29
Valenti, J. A., & Fischer, D. A. 2005, ApJS, 159, 141
Vernet, J., Dekker, H., D'Odorico, S., et al. 2011, A&A, 536, A105
Vigan, A., Lopez, M., El Morsy, M., et al. 2022, SPIE Conf. Ser., 12185, 121850S
Vos, J. M., Allers, K. N., Biller, B. A., et al. 2018, MNRAS, 474, 1041
Vos, J. M., Biller, B. A., Allers, K. N., et al. 2020, AJ, 160, 38
Vrba, F. J., Henden, A. A., Luginbuhl, C. B., et al. 2004, AJ, 127, 2948
Wang, J. J., Ruffio, J.-B., Morris, E., et al. 2021, AJ, 162, 148
Wells, M., Pel, J. W., Glasse, A., et al. 2015, PASP, 127, 646
Whiteford, N., Faherty, J. K., Burningham, B., et al. 2025, ApJ, Submitted
Wilson, J. C., Miller, N. A., Gizis, J. E., et al. 2003, in IAU Symposium, 211, Brown Dwarfs, ed. E. Martín, 197
Zapatero Osorio, M. R., Béjar, V. J. S., Miles-Páez, P. A., et al. 2014, A&A, 568, A6
Zhang, Y., Snellen, I. A. G., Bohn, A. J., et al. 2021a, Nature, 595, 370
Zhang, Z., Liu, M. C., Best, W. M. J., Dupuy, T. J., & Siverd, R. J. 2021b, ApJ, 911, 7
Zhang, Z., Liu, M. C., Marley, M. S., Line, M. R., & Best, W. M. J. 2021c, ApJ, 916, 53
Zhang, Z., Liu, M. C., Marley, M. S., Line, M. R., & Best, W. M. J. 2021d, ApJ, 921, 95
Zhang, Z., Mollière, P., Fortney, J. J., & Marley, M. S. 2025, arXiv e-prints [arXiv:2502.18559]
Zhou, Y., Apai, D., Schneider, G. H., Marley, M. S., & Showman, A. P. 2016, ApJ, 818, 176
Zhou, Y., Bowler, B. P., Morley, C. V., et al. 2020, AJ, 160, 77
Zhou, Y., Bowler, B. P., Apai, D., et al. 2022, AJ, 164, 239
Zuckerman, B., Song, I., & Webb, R. A. 2001, ApJ, 559, 388
Zuckerman, B., Song, I., & Bessell, M. S. 2004, ApJ, 613, L65
Zuckerman, B., Bessell, M. S., Song, I., & Kim, S. 2006, ApJ, 649, L115

[1] NASA-Goddard Space Flight Center, Greenbelt, MD 20771, USA
[2] Instituto de Estudios Astrofísicos, Facultad de Ingeniería y Ciencias, Uni. Diego Portales, Av. Ejército 441, Santiago, Chile
[3] Millennium Nucleus on Young Exoplanets and their Moons (YEMS), Santiago, Chile
[4] Univ. Grenoble Alpes, CNRS, IPAG, 38000 Grenoble, France
[5] Max-Planck-Institut für Astronomie, Königstuhl 17, 69117 Heidelberg, Germany
[6] Laboratoire Lagrange, Université Cote d'Azur, CNRS, Observatoire de la Cote d'Azur, 06304 Nice, France
[7] Maison de la Simulation, CEA, CNRS, Univ. Paris-Sud, UVSQ, Université Paris-Saclay, 91191 Gif-sur-Yvette, France
[8] Department of Astronomy, University of Texas at Austin, Austin, TX, USA
[9] LESIA, Observatoire de Paris, Université PSL, CNRS, Sorbonne Université, Univ. Paris Diderot, Sorbonne Paris Cité, 5 place Jules Janssen, 92195 Meudon, France
[10] Department of Astrophysics, American Museum of Natural History, Central Park West at 79th Street, NY 10024, USA
[11] Planétarium de Montréal, Espace pour la Vie, 4801 av. Pierre-de Coubertin, Montréal, Québec, Canada
[12] Trottier Institute for Research on Exoplanets, Université de Montréal, Département de Physique, C.P. 6128 Succ. Centre-ville, Montréal, QC H3C 3J7, Canada
[13] Aix Marseille Univ, CNRS, CNES, LAM, Marseille, France
[14] European Southern Observatory, Karl Schwarzschild-Straße 2, D-85748 Garching bei München, Germany
[15] Institute for Astronomy The University of Edinburgh Royal Observatory Blackford Hill Edinburgh EH9 3HJ UK
[16] Department of Astronomy and Carl Sagan Institute, Cornell University, 122 Sciences Drive, Ithaca, NY 14853, USA
[17] Astrophysics Group, School of Physics and Astronomy, University of Exeter, Exeter EX4 4QL, UK
[18] AURA for the European Space Agency (ESA), ESA Office, Space Telescope Science Institute, 3700 San Martin Drive, Baltimore, MD 21218 USA
[19] Centro de Astrofísica y Tecnologías Afines (CATA), Casilla 36-D, Santiago, Chile
[20] Observatoire de Genève, Département d'Astronomie, Université de Genève, Chemin Pegasi 51b, 1290 Versoix, Switzerland
[21] Institute for Astronomy, University of Hawai'i at Mānoa, 2680 Woodlawn Drive, Honolulu, HI 96822, USA
[22] Department of Physics & Astronomy, Johns Hopkins University, Baltimore, MD 21218, USA
[23] Division of Space Research and Planetary Sciences, Physics Institute, University of Bern, Gesellschaftsstr. 6, 3012 Bern, Switzerland
[24] Center for Space and Habitability, University of Bern, Gesellschaftsstr. 6, 3012 Bern, Switzerland
[25] Fakultät für Physik, Universität Duisburg-Essen, Lotharstraße 1, 47057 Duisburg, Germany
[26] Departamento de Astronomía, Universidad de Chile, Camino el Observatorio 1515, Las Condes, Santiago, Chile
[27] Department of Astronomy & Astrophysics, University of California, Santa Cruz, CA 95064, USA
[28] Department of Physics & Astronomy, University of Rochester, Rochester, NY 14627, USA

Appendix A: Observing log

Table A.1 presents the observing log for each observed epoch of each object in the X-SHYNE library.

Table A.1. Table A.1. Obs. log

Target	Date [yyyy-mm-dd]	⟨ Seeing ⟩ ["]	Airmass	Target	Date [yyyy-mm-dd]	⟨ Seeing ⟩ ["]	Airmass
2MASS 0030	2018-07-28	0.86	1.20	2MASS 2139	2023-06-06	0.49	1.13
-	2018-08-16	0.60	1.08	2MASS 2206	2018-06-01	0.70	1.08
2MASS 0045	2018-10-09	1.12	1.34	2MASS 2244	2018-07-23	0.74	1.44
-	2018-10-17	0.68	1.35	2MASS 2322	2018-06-26	0.71	1.27
2MASS 0046	2019-07-15	0.65	1.28	2MASS 2354	2019-10-11	0.80	1.49
2MASS 0103	2019-10-10	0.68	1.62	PSO 057	2018-10-17	1.00	1.33
-	2019-10-11	0.55	1.40	-	2018-10-18	0.70	1.33
2MASS 0153	2018-10-08	0.59	1.39	-	2018-10-22	0.74	1.32
-	2018-10-17	0.79	1.37	-	2018-10-30	0.44	1.33
-	2018-10-18	0.68	1.37	PSO 071	2018-10-30	0.39	1.03
2MASS 0219 b	2018-10-21	0.93	1.16	-	2018-10-30	0.34	1.04
2MASS 0249 c	2019-10-10	0.74	1.10	-	2018-10-30	0.62	1.10
-	2019-10-10	0.88	1.20	-	2018-10-31	0.63	1.08
-	2019-10-11	0.70	1.08	PSO 318	2018-06-20	0.64	1.14
-	2019-10-11	1.02	1.17	-	2018-06-27	0.70	1.04
2MASS 0326	2018-10-21	0.82	1.18	PSO 319	2018-05-30	0.79	1.02
2MASS 0342	2018-10-08	0.68	1.39	SDSS 1110	2018-04-29	0.94	1.13
2MASS 0355	2019-09-10	0.76	1.25	-	2018-05-27	0.67	1.12
2MASS 0508	2020-01-14	0.65	1.02	-	2018-05-28	0.62	1.20
2MASS 0512	2018-10-31	0.48	1.01	SIMP 0136	2018-11-16	0.89	1.23
2MASS 0518	2018-11-27	0.68	1.25	ULAS 0047	2023-08-01	1.12	1.32
2MASS 0616	2019-11-17	0.67	1.09	-	2023-08-01	0.97	1.38
2MASS 0723	2020-02-06	1.01	1.02	ULAS 1316	2023-04-11	0.62	1.30
2MASS 1021	2018-04-28	0.60	1.09	-	2023-04-11	1.00	1.31
-	2018-05-04	0.72	1.13	-	2023-03-30	1.10	1.14
2MASS 1119	2019-04-15	0.94	1.04	VHS 1256 b	2018-05-28	0.74	1.17
2MASS 1147	2018-06-16	1.50	1.16	-	2018-05-28	0.68	1.05
2MASS 1148	2018-04-29	0.53	1.14	WISE 0241	2022-12-30	0.75	1.06
-	2018-04-29	0.57	1.04	-	2023-01-19	0.94	1.17
2MASS 1207	2018-04-28	0.56	1.09	-	2023-02-03	0.86	1.43
2MASS 1213	2019-04-15	0.68	1.08	WISE 0528	2018-10-22	0.62	1.21
2MASS 1425	2018-06-19	1.56	1.14	-	2018-10-26	0.58	1.21
2MASS 1521	2023-04-10	0.66	1.24	-	2018-10-26	0.73	1.27
-	2023-04-10	0.66	1.41	WISE 0819	2022-12-16	0.86	1.20
-	2023-05-02	0.44	1.57	WISE 2216	2019-06-05	0.72	1.42
2MASS 1826	2019-04-18	1.08	1.08	-	2019-06-16	0.97	1.41
-	2019-04-18	1.32	1.08	-	2019-07-11	0.53	1.48
-	2019-04-30	0.87	1.10	-	2019-07-12	0.82	1.44
2MASS 2104	2019-05-03	0.59	1.20	-	2019-07-15	0.68	1.45
-	2019-07-11	0.46	1.08	-	2019-07-15	0.64	1.42
-	2019-07-12	0.63	1.05				

Appendix B: Zooms into the X-SHYNE library of spectra

Figures B.1, B.2, B.3, B.4, and B.5 illustrate the richness of the X-SHYNE spectra through zoomed-in views of the visible (0.60-0.85 µm), Y(0.85-1.10 µm), J (1.10-1.35 µm), H (1.42-1.81 µm), and K (1.96-2.48 µm) bands. Most of the detected atomic and molecular features are highlighted.

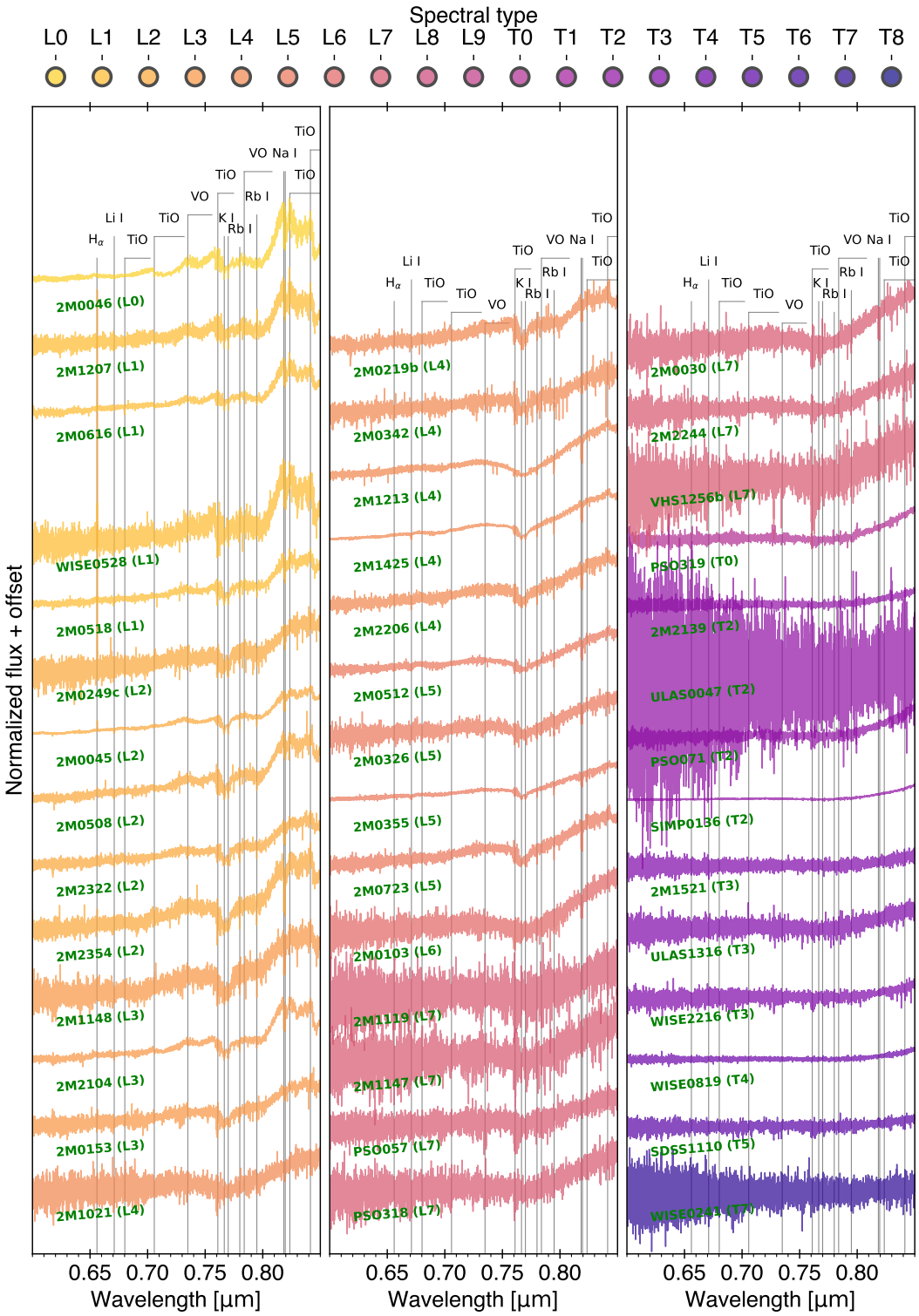

Fig. B.1. Same than the Figure 1 with a zoom between 0.60 and 0.85 µm. The main spectral features are identified.

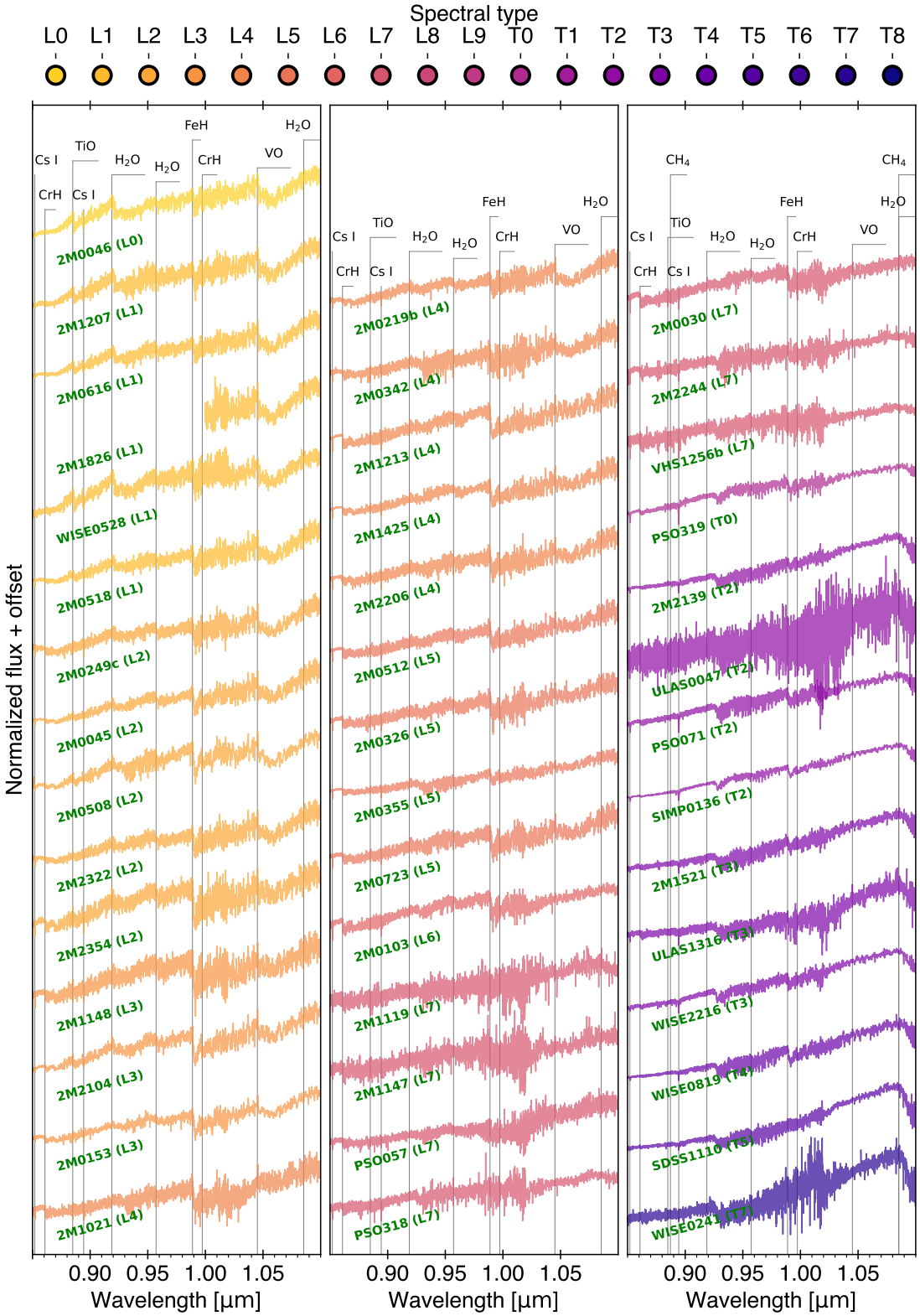

Fig. B.2. Same than the Figure 1 with a zoom between 0.85 and 1.10 μm. The main spectral features are identified.

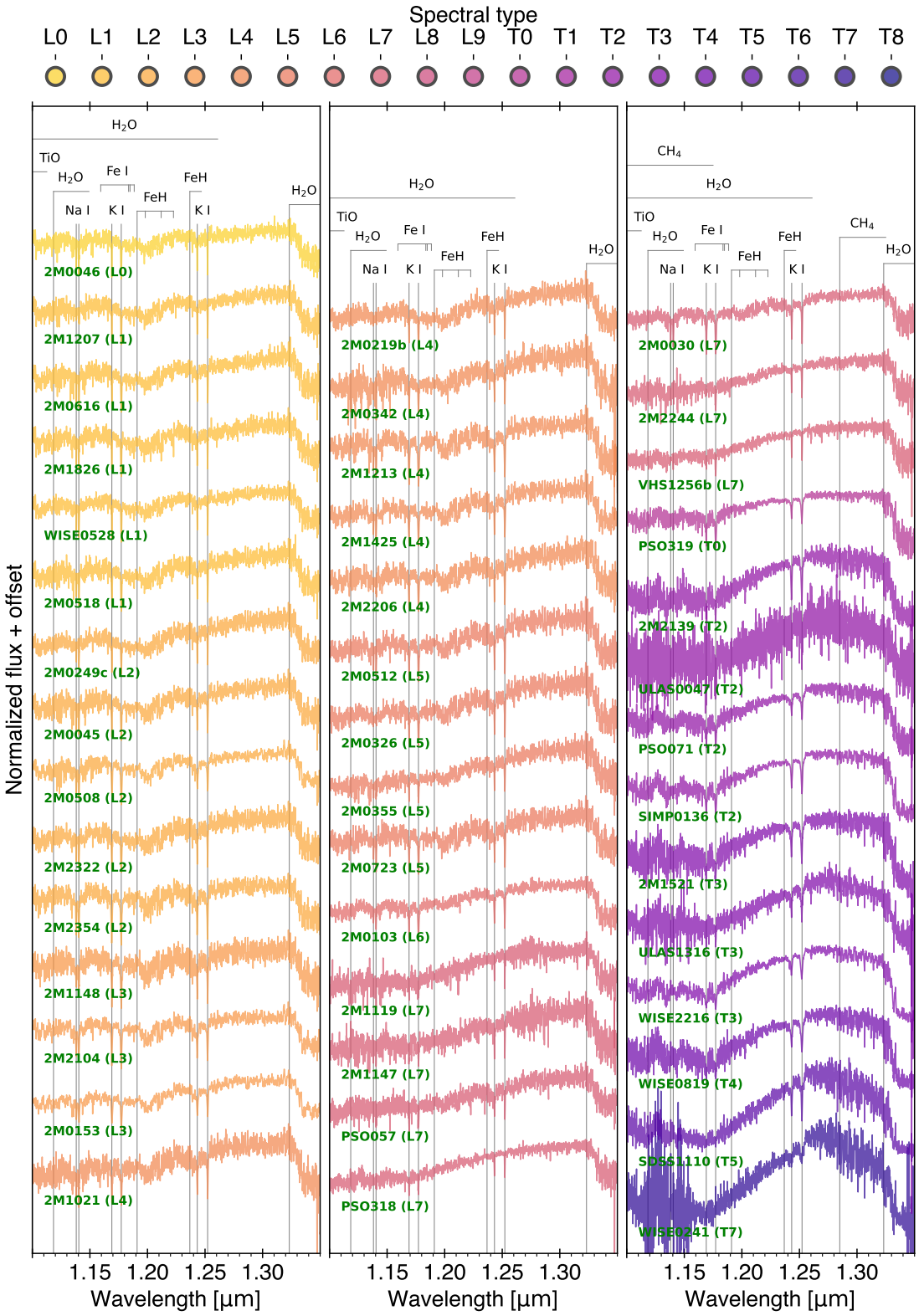

Fig. B.3. Same than the Figure 1 with a zoom between 1.10 and 1.35 μm. The main spectral features are identified.

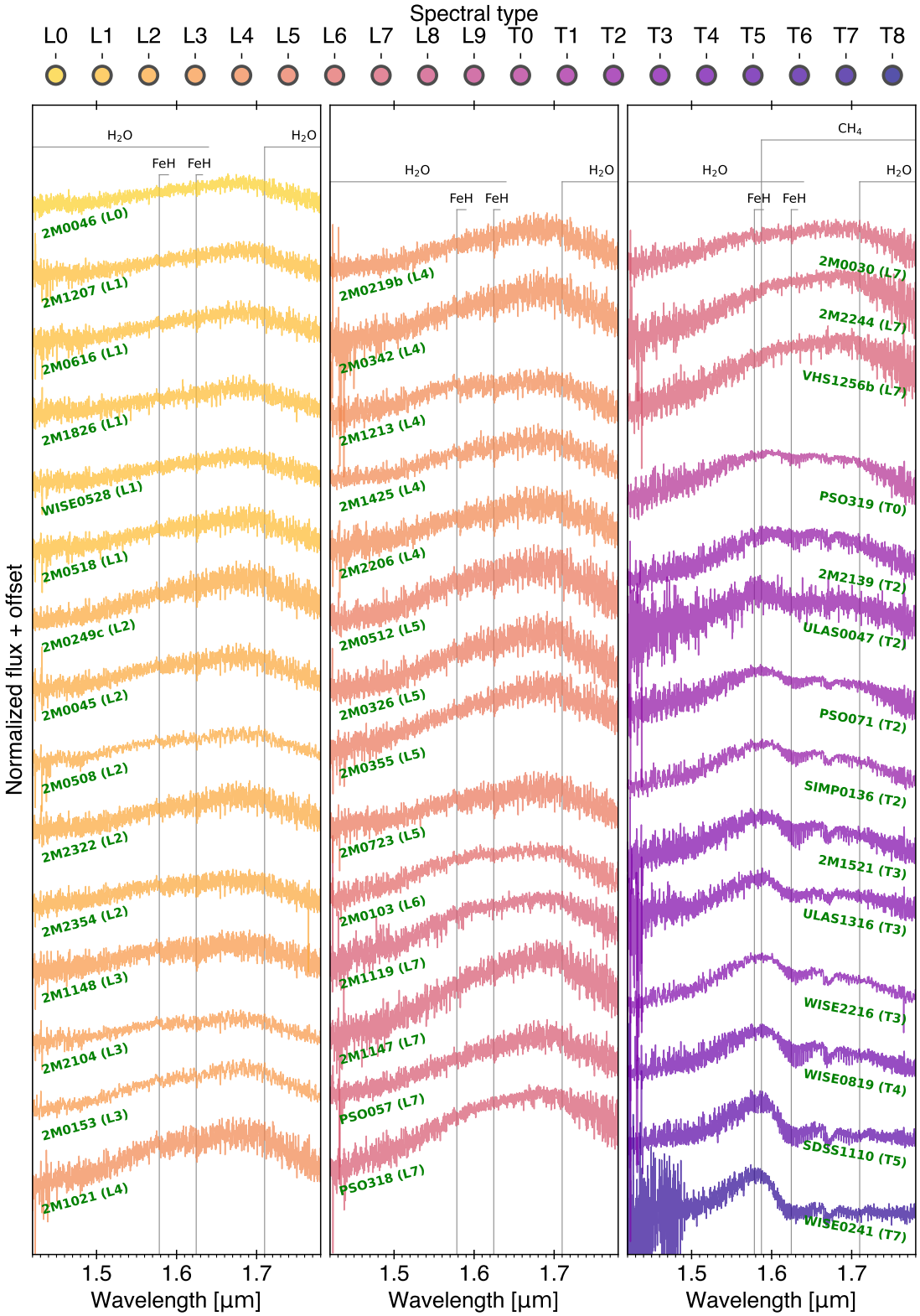

Fig. B.4. Same than the Figure 1 with a zoom between 1.42 and 1.81 μm. The main spectral features are identified.

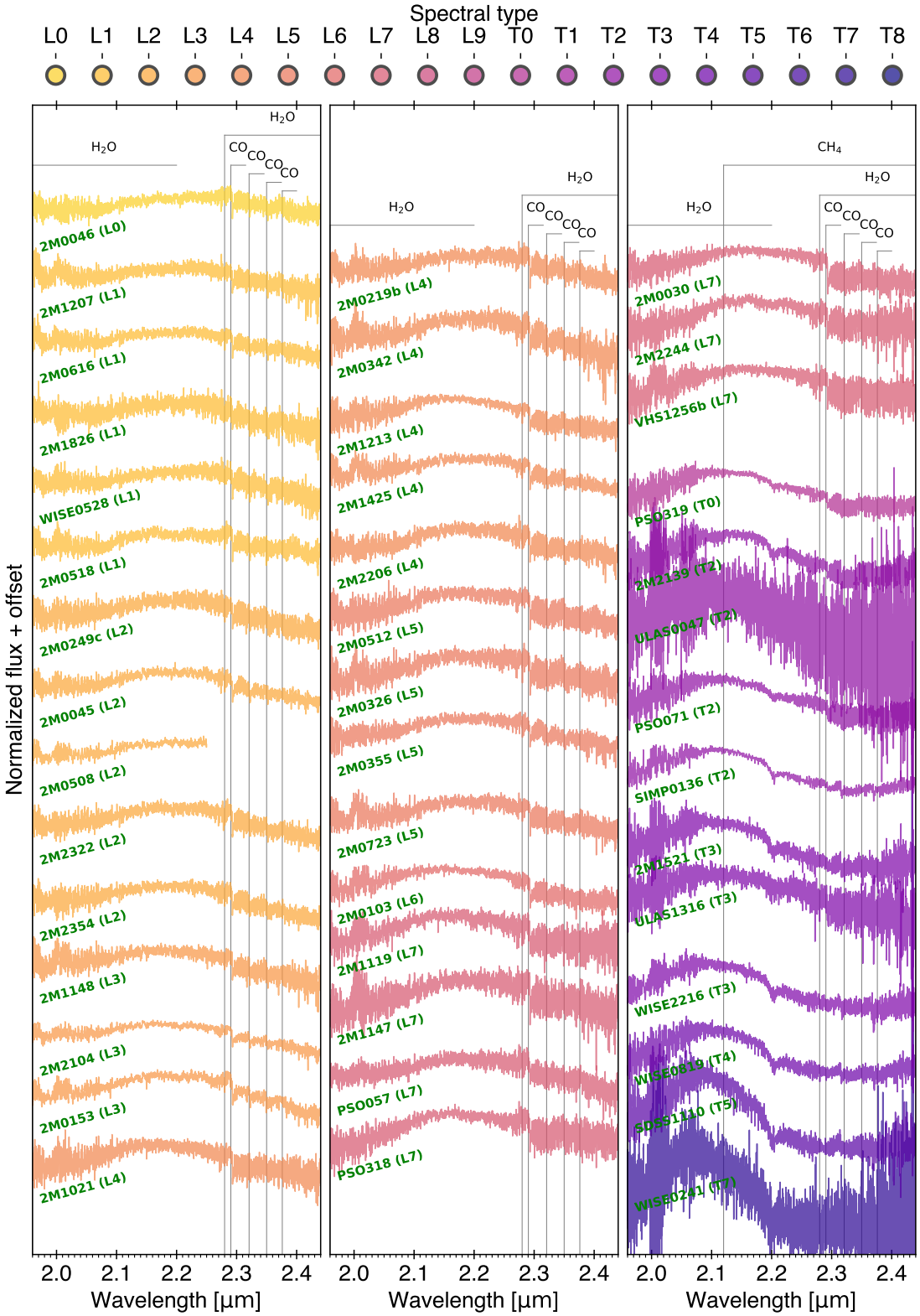

Fig. B.5. Same than the Figure 1 with a zoom between 1.96 and 2.48 μm. The main spectral features are identified. For this plot, the spectra have been normalized with their integrated flux between 1.5 and 1.8 μm.

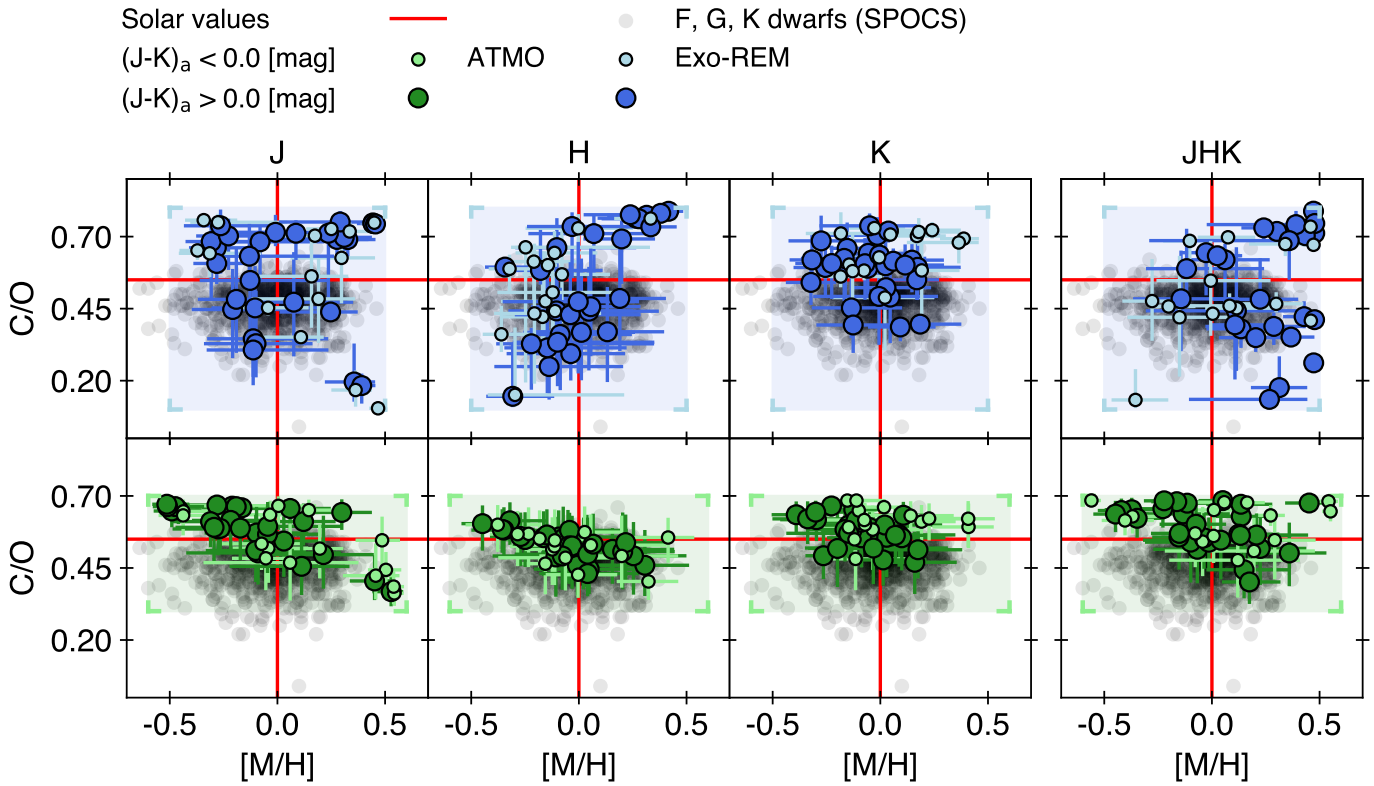

Fig. C.1. Same as in Figure 12 but for each wavelength ranges.

Appendix C: [M/H] and C/O ratio for every fitting configurations

Figure C.1 illustrates the [M/H] and C/O estimates derived from the J, H, and K bands, as well as their combination. The K band provides less dispersed values, likely due to the CO overtones at ~2.3 µm, which are known to be particularly sensitive to the C/O ratio.